INVESTIGATION OF SCREEN-PRINTED AND EVAPORATED METAL CONTACTS ON BORON IMPLANTED EMITTER

A THESIS SUBMITTED TO
THE GRADUATE SCHOOL OF NATURAL AND APPLIED SCIENCES
OF
MIDDLE EAST TECHNICAL UNIVERSITY

BY

EGE ÖZMEN

IN PARTIAL FULFILLMENT OF THE REQUIREMENTS
FOR
THE DEGREE OF MASTER OF SCIENCE
IN
MICRO AND NANOTECHNOLOGY

AUGUST 2021

Approval of the thesis:

INVESTIGATION OF SCREEN-PRINTED AND EVAPORATED METAL CONTACTS ON BORON IMPLANTED EMITTER

submitted by **EGE ÖZMEN** in partial fulfillment of the requirements for the degree of **Master of Science** in **Micro and Nanotechnology, Middle East Technical University** by,

Prof. Dr. Halil Kalıpçılar
Dean, Graduate School of **Natural and Applied Sciences** _____

Prof. Almila Güvenç Yazıcıoğlu
Head of the Department, **Micro and Nanotechnology, METU** _____

Prof. Dr. Raşit Turan
Supervisor, **Physics, METU** _____

Assoc. Prof. Serdar Kocaman
Co-Supervisor, **Electrical and Electronics Eng., METU** _____

Examining Committee Members:

Prof. Dr. H. Emrah Ünalan
Metallurgical and Materials Eng., METU _____

Prof. Dr. Raşit Turan
Physics, METU _____

Prof. Dr. H. Mehmet Parlak
Physics, METU _____

Assoc. Prof. Dr. Mustafa Kulakcı
Physics, Eskişehir Technical University _____

Assoc. Prof. Dr. Emre Yüce
Physics, METU _____

Date: 27.08.2021

I hereby declare that all information in this document has been obtained and presented in accordance with academic rules and ethical conduct. I also declare that, as required by these rules and conduct, I have fully cited and referenced all material and results that are not original to this work.

Name Last name : Ege Özmen

Signature :

ABSTRACT

INVESTIGATION OF SCREEN-PRINTED AND EVAPORATED METAL CONTACTS ON BORON IMPLANTED EMITTER

Özmen, Ege
Master of Science, Micro and Nanotechnology
Supervisor: Prof. Dr. Raşit Turan
Co-Supervisor: Assoc. Prof. Serdar Kocaman

August 2021, 65 pages

Due to advantages in device manufacturing and the low cost of ownership, crystalline silicon (c-Si) solar cells fabricated on p-type wafers continue to dominate the photovoltaic (PV) market. Studies on n-type Czochralski (CZ) substrates have shown that they are more desirable for terrestrial applications than p-type substrates due to superior material and performance advantages such as higher minority carrier lifetime and easier surface passivation, absence of light-induced degradation (LID), and low sensitivity to metallic impurities. With these advantages, n-type CZ-based c-Si solar cells hold great potential in the future PV industry. However, various difficulties in device processing and higher wafer cost are still the major obstacles in penetrating the n-type solar cells into the commercial market. In dealing with these difficulties, new processes like ion implantation are being considered to replace the existing ones to simplify the process conditions and lower the cost.

This thesis aims to optimize the activation temperature and duration of the boron implanted silicon with metal contacts fabricated by screen printing and e-beam evaporation. In order to understand the uniformity of the ion implantation, sheet resistance measurements were carried out. Al_2O_3/SiN_x stack was used for passivation and ARC. Also, deeper boron concentration leads to lower contact resistivity is tested with e-beam evaporated and screen-printed metal contacts with contact resistivity values measured using Transmission Line Measurement (TLM). We have shown that successful metal contact to ion-implanted Si can be formed using both techniques. This thesis presents excessive process information and results for the screen-printed and e-beam evaporated samples onto the boron implanted silicon.

Keywords: Boron implanted silicon, contact resistivity, e-beam evaporation, screen-printing

ÖZ

BOR YERLEŞTİRİLMİŞ SİLİSYUM ÜZERİNDEKİ SERİGRAFİK VE BUHARLAŞMIŞ METAL KONTAKLARIN İNCELENMESİ

Özmen, Ege
Yüksek Lisans, Mikro ve Nanoteknoloji
Tez Yöneticisi: Prof. Dr. Raşit Turan
Ortak Tez Yöneticisi: Doç. Dr. Serdar Kocaman

Ağustos 2021, 65 sayfa

Cihaz üretimindeki avantajlar ve düşük maliyet nedeni ile p-tipi dilimler üzerinde üretilen kristal silikon (c-Si) güneş hücreleri, fotovoltaik (PV) pazarına hakim olmaya devam ediyor. Öte yandan, n-tipi Czochralski (CZ) alttaşlar üzerinde yapılan çalışmalar, daha yüksek azınlık taşıyıcı ömrü, daha kolay yüzey pasivasyonu, ışık kaynaklı bozulmanın olmaması ve metalik safsızlıklara kara düşük hassasiyet gibi üstün malzeme ve proses avantajlarından dolayı karasal uygulamalar için p-tipi alttaşlara göre avantajlı olduklarını göstermiştir. Bu avantajlarla, n-tipi CZ tabanlı c-Si güneş hücreleri, geleceğin PV endüstrisinde büyük bir potansiyele sahiptir. Öte yandan, n-tipi hücre üretiminde bir çok zorluklar ve yükske maliyet söz konusudur. Bu zorlukları aşmak üzere alternatif prosesleri içeren çalışmalar yürütülmektedir. İyon ekme (Ion Implantation) katkılama işlemi içinkullanılan ve olldukça umut veren alternatif proseslerden bir tanesidir.

Bu tezin amacı, elek baskı ve e-demeti buharlaştırma yöntemi ile oluşturulmuş metal kontaklarla boron ekilmiş silisyum katkılama aktivasyon sıcaklığını ve süresini optimize etmektir. İyon ekimin homojenliğini anlamak için tabaka direnci ölçümleri yapılmıştır. Al_2O_3/SiN_x katmanlı yapısı sırasıyla pasivasyon ve yansıma önleyici kaplama yöntemleri için kullanılmıştır. Ayrıca, daha derin bor konsantrasyonunun daha düşük temas direncine yol açtığı gerçeği, İletim Hattı Ölçümü (TLM) kullanılarak e-demeti ve elek baskı yöntemi ile üretilmiş metal kontaklarla kontak direnci değerleri ile test edilmiştir. Bu tez, boron ekilmiş Si üzerine metal kontak oluşturma konusunda ayrıntılı deneysel çalışmaların sonuçlarını sunmaktadır.

Anahtar Kelimeler: Boron ekilmiş Si, kontak direnci, e-demeti buharlaştırma, elek baskı

To my grandma, Neriman Atatekin…

ACKNOWLEDGMENTS

I would like to thank my supervisor Prof. Dr. Raşit Turan for his invaluable help, his patience, guidance, and criticism. His encouragement not only made me complete this research but also made me enthusiastic about my work. I want to thank my co-supervisor, Assoc. Prof. Serdar Kocaman for his support and understanding.

The biggest gratitude goes to the Gence Bektaş. When I needed encouragement, he was always there for me and acted like a brother. His help through this work was remarkable and his guidance was always helpful. His enthusiasm made me attached to this study even in my darkest hours. Without him, this thesis would not be happened. I would also thank my GÜNAM GPVL family, Dr. Bülent Arıkan, Sümeyye Koçak Bütüner, Hasan Asav, Hasan Hüseyin Canar, Ahmet Emin Keçeci, Furkan Çiçek, Batuhan Taş, and Murat Aynacıoğlu for all the help they gave.

I would like to show my gratitude to my behind the camera people, Selen Karadeniz, Ukte Yüksel, Sena Dumanoğlu, Beril Bul, and Devin Aykasım, for their spare time entertainments throughout this study. When I thought I couldn't do it, they had always supported me and listened to me. Without them, I would lose my mind. I want to thank Oğuzhan Burak Issı, who made me feel loved and supported constantly. With him by my side, I can achieve every success in life and I'm so grateful he's in my life.

Finally, I would like to thank to my family. My mother and my father are always going to be my luck in this life. My brother, who is a master ninja and a great intellectual, is my best friend and my rockstar. His wife, my chess champion sister-in-law, was the perfect person to talk about through this study. Their support was unlimited from the beginning of my bachelor to end of my master's degree.

This work is partially funded by Scientific and Technological Research Council of Turkey under grant numbers TUBITAK 20AG002 and 113G050.

TABLE OF CONTENTS

LIST OF TABLES

LIST OF FIGURES

NOMENCLATURE

Al	Aluminum
Al_2O_3	Aluminum oxide
ALD	Atomic layer deposition
ARC	Anti-reflective coating
CB	Conduction band
c-Si	Crystalline silicon
Cz	Czochralski
E	Electric field
ECV	Electrochemical vapor deposition
E_{PH}	Photon energy
E_G	Energy band gap
eV	Electron volt
FF	Fill factor
GW	Gigawatt
HF	Hydrofluoric
I_0	Saturation current
I_L	Light generated current
I_{SC}	Short circuit current
I-V	Current-Voltage
L_T	Transfer length

MS	Metal-Semiconductor
n_i	Intrinsic carrier concentration
PECVD	Plasma enhanced chemical vapor deposition
PV	Photovoltaic
R_C	Contact resistance
R_S	Series resistance
R_{SH}	Shunt resistance
SiN_x	Silicon nitride
SiO_2	Silicon dioxide
SRH	Shockley-Read-Hall
SQ	Shockley-Quessier
TLM	Transmission Line Measurement
V	Voltage
VB	Valence band
V_{bi}	Built-in potential
V_{MPP}	Voltage at maximum power point
V_{OC}	Open circuit voltage
ρ_C	Specific contact resistivity
η	Cell conversion efficiency
Φ_B	Schottky barrier potential

CHAPTER 1

INTRODUCTION

1.1 Solar Energy in the World and Turkey

As the human population increases, our ecological footprint increases, leading to a diminishment of our vital resources. Also, traditional fossil fuels are causing fatal environmental problems such as climate change, air pollution, and global warming. Renewable energies should replace fossil fuels to deal with the political, economic, and environmental challenges we face in that area. Solar energy, as an endless source, has the furthest potential in this direction.

According to International Renewable Energy Agency (IRENA), the total electricity generated from renewables was 6586 TWh in 2018. 9% of this was from solar energy. Renewable electricity generation increased by 6.1% in 2017. Solar energy overtook bioenergy in 2018 and became the third-largest source of renewable electricity generation, increasing 28%. In Turkey, 28079 facilities used photovoltaic solar energy as their primary source in 2018 (International Renewable Energy Agency, 2020).

Global solar photovoltaic capacity additions are anticipated to reach about 107 GW in 2020, according to the International Energy Agency's (IEA) 2020 forecast, reflecting steady increase from 2019. In 2020, the US was predicted to increase utility-scale additions by 3%, while China is expected to raise its photovoltaic capacity by over 33% than in 2019. IEA data showed that construction activity for utility-scale projects slowed from March through April due to the ongoing pandemic but rapidly regained speed in mid-May. It is expected that global PV additions will accelerate between 2023-2025 as the global economy improves. Coupled with the

government, market drivers are expected to support global photovoltaic expansion (Bahar & Bojek, 2020).

In the graph presented in Figure 1 below, one can see Turkey's solar photovoltaic capacity and production increase. The rapid increase after 2015 in the PV installation in Turkey is seen.

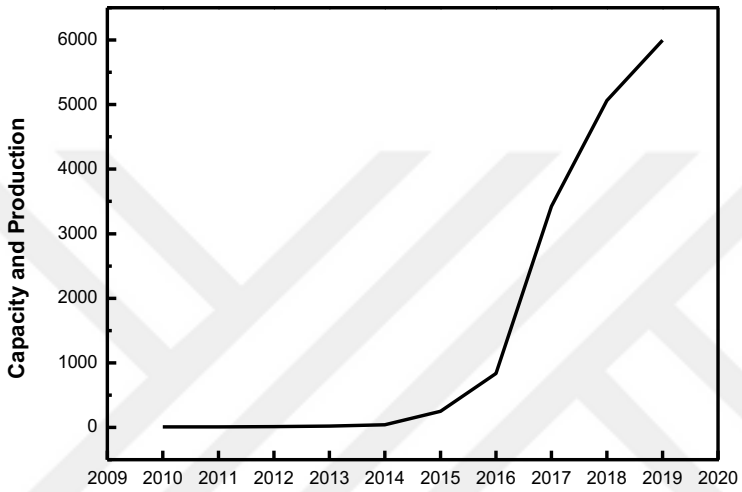

Figure 1. Capacity and Production Growth of Turkey through years adapted from IRENE 2020 Report.

1.2 History of Photovoltaics

Solar energy was always an attention grabber for humans, even in the early ages when it was discovered that the sun hits warmer than the shade. However, the discovery of the photovoltaic effect is not too distant from our time. The first person who saw the photovoltaic effect was Edmond Becquerel, which resulted from scientific curiosity. He experimented with a cell comprised of metal electrodes in a conducting fluid in 1839 and discovered that it created more electricity when the device was exposed to light, but he could not explain why. Willoughby Smith found that selenium could be used as a photoconductor in 1873, and Grylls Adams and

Richard Evans Day imitated Becquerel's selenium experiment in 1876, which yielded the same result (Nelson, 2003).

Fifty years later, the first working selenium solar cell was created by Charles Fritts with less than 1% efficiency (Meyers, 2014). Goldman and Brodsky researched the photovoltaic properties of metal-semiconductor surfaces in 1914, and they discovered a barrier layer in solar devices. Later, Schottky gave a theoretical explanation for the barrier layer (Sah, 2006). Jan Czochralski produced a method to grow single metal crystals, which describes how we produce single c-Si (Nishinaga, 2015). The development of diffused junctions enhanced the efficiency of solar cells. Bell Laboratories recognized that Si is far more efficient than selenium and developed the first Si solar cell with boron diffused junction in 1954, ushering in a new era in solar technology (Chodos, 2009). After that, Western Electric licensed commercial solar cell technology with 2% efficiency and $1,785/watt. In 1957, Mohamed M. Atalla developed the surface passivation process for Si solar cells at the Bell Laboratories. Hoffman Electronics introduced grid contact usage in 1959, and the efficiency of this solar cell was reached 10%, and by 1960, they achieved 14% efficiency. Sharp Corporation, in 1963, produced practical Si photovoltaic modules. In 1972, the first laboratory dedicated to photovoltaic research and development was established at the University of Delaware. In 1977, production from the photovoltaic cells reached 500 kW, and the production increased to 21.3 megawatts in 1983.

From 1941 to 1983, the development and efficiency of full-area Si solar cells can be seen in Table 1 below (Green, 2009).

Table 1. Cell Structures and efficiency results throughout the years adapted from Green, 2009.

Date	Efficiency (%)	Cell Structure	Organization
March 1941	<1	Melt grown junction	Bell Laboratories
March 1952	~1	He bombardment	Bell Laboratories
December 1953	~4.5	Li diffused wraparound	Bell Laboratories
January 1954	~6	B diffused wraparound	Bell Laboratories
November 1954	~8	B diffused wraparound	Bell Laboratories
May 1955	~11	B diffused wraparound	Bell Laboratories
December 1957	~12.5	0.5x2 cm^2 B diffused	Hoffman Electronics
August 1959	~14	Grid-contact B diffused	Hoffman Electronics
August 1961	~14.5	B diffused, AR coated, gridded	Commercial, USASRDL
January 1973	~15.3	Violet Cell	Comsat Laboratories
September 1974	~17.3	Textured, non-reflecting	Comsat Laboratories
September 1983	18.1	MINP cell	University of NSW

Table 2. Reported efficiencies of different solar cells adapted from Green, 2009.

Date	Reported Efficiency	Area	Cell Description
01.1983	16.5	Total Area	ORNL
05.1983	17.1	Total Area	ASEC
08.1983	17.1	Aperture Area	Westinghouse
09.1983	18.0	Total Area	Spire textured
	18.7	Total Area	UNSW MINP
12.1993	19.1	Total Area	UNSW PESC
05.1985	19.8	Aperture Area	UNSW PESC
10.1985	20.0	Aperture Area	UNSW µg PESC
07.1986	20.6	Designed Illumination Area	UNSW µg PESC
04.1988	21.4	Aperture Area	UNSW µg PESC
09.1988	22.3	Aperture Area	Stanford
06.1989	23.2	Aperture Area	UNSW PERC
12.1989	23.0	Aperture Area	UNSW PERL
02.1990	24.2	Aperture Area	UNSW PERL
03.1994	23.5	Aperture Area	UNSW PERL
09.1994	24.0	Aperture Area	UNSW PERL
02.1998	24.4	Designed Illumination Area	UNSW PERL
11.1998	24.5	Designed Illumination Area	UNSW PERL
03.1999	24.7	Designed Illumination Area	UNSW PERL

From Table 2 above, one can see the history of solar cell improvement of >1 cm^2 area over the modern era normalized to present standard test conditions.

When it comes to 1999, the photovoltaic capacity already reached 1000 megawatts. Until 2015, the price has drastically decreased, around $0.61/watt, when the installation amount has increased up to 65 Gigawatts (GW).

The best research-cell efficiencies over the years are shown in Figure 2.

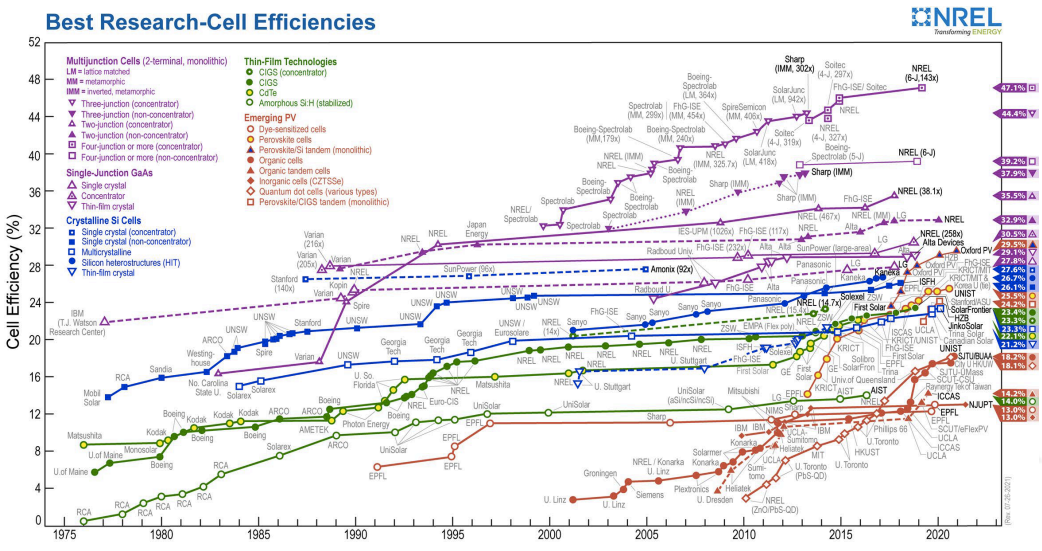

Figure 2. The best research cell efficiencies from NREL.

1.3 n-type Cell History

Although p-type solar cells dominate the PV industry, n-type solar cells are appealing because of their material features, including the absence of boron-oxygen-related defects and a higher tolerance for metal impurities (Fe, Al, Co, Ni) (Aissa et al., 2015). As a result, companies like Sanyo and SunPower, the top ones, started to manufacture high-efficiency modules using n-type substrates. While Sanyo produces HIT solar cells, SunPower manufactures IBC solar cells, Yingli Green Energy started manufacturing PANDA and bifacial n-Pasha solar cells, all of which are based on n-type (Ur Rehman & Lee, 2013). High efficiencies are reported from these companies,

and along with the new improvements and results, n-type solar cells will be a significant contributor to the market in the upcoming years.

JinkoSolar Holding Co Ltd reported in 2020 that full area contact-passivated solar cells with a maximum efficiency of 24.79% had broken the global record for a big area n-type monocrystalline Si solar cell. This discovery was confirmed by the Institute for Solar Energy Research in Hamelin (ISFH) in Germany (Jinko Solar, 2020).

1.4 Solar Cell Operation Principles

1.4.1 Basics of Semiconductors

Materials can be classified according to their electrical and optical properties, determined by the electronic band structure as shown in Figure 3. A semiconductor material class has a moderate band gap leading to an electrical conductivity between an insulator and a conductor. There is various type of semiconductors having different electrical optical and mechanical properties. Among them, Si is perhaps the most important one which dominates today's microelectronics and photovoltaics. By introducing impurities, called doping, into the semiconductor materials, their conductivity can be changed. Two differently doped regions in semiconductors create a so-called junction.

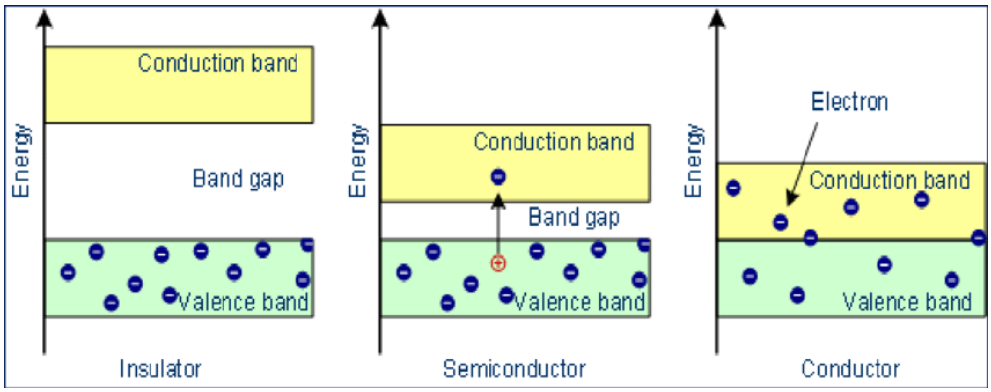

Figure 3. Energy gap for conductors, semiconductors, and insulator materials (Obeid, 2010).

Material properties of a semiconductor are defined by its energy band structure which is usually shown in the momentum space. The energy band structure of three major semiconductors is shown in Figure 4.

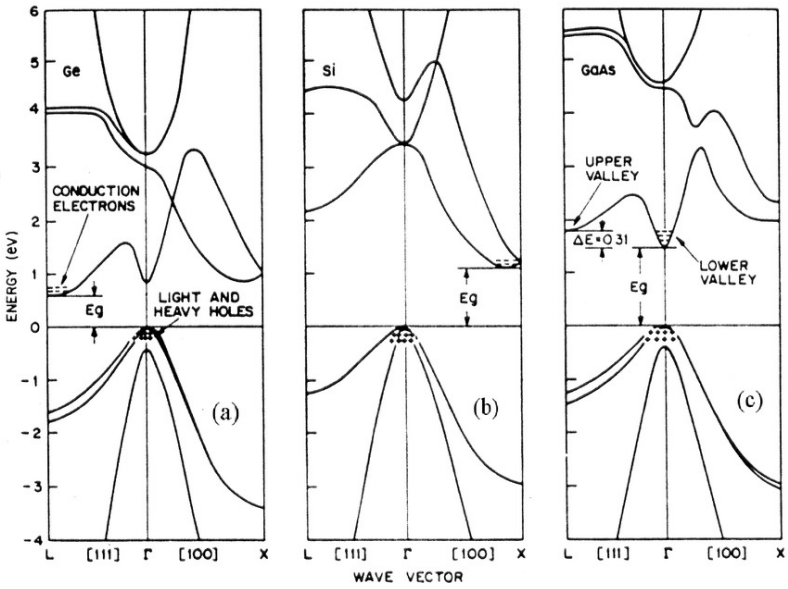

Figure 4. Energy band diagrams of (a) Germanium, (b) Silicon, and (c) Gallium Arsenide (Bera, 2011).

The bandgap of the materials is seen in these examples. Silicon and Germanium have indirect bandgap material with conduction band (CB) minimum and valence band (VB) maximum at different momentum positions (Figures 4a and 4b). GaAs has a direct bandgap structure having the extremum points at the same k-value. With its

indirect band structure, Si is a poor light absorber, and for this reason, solar cells made of Si should be thick enough to make sure the absorption of the whole spectrum.

The semiconductors with no doping are called intrinsic semiconductors. The free charge carrier concentration is determined by the thermal excitation of electrons from the valence band in the CB. The intrinsic concentration (n_i) is defined as the number of CB electrons and valence band holes. If the bandgap is large, the intrinsic carrier concentration is low since it is more difficult to excite an electron across the bandgap. Alternatively, increasing the temperature increases the intrinsic carrier concentration since electrons are more likely to excite through the bandgap.

Doping changes the balance of electrons and holes in a semiconductor material. N-type semiconductors are made by adding dopant atoms into Si that have one extra valence electron than Si. A p-type semiconductor material is made with dopant atoms that have one valence electron less than Si. When it comes to doping, one of the carriers always has a larger concentration than the other, and the carrier with the higher concentration is known as the majority carrier, while the carrier with the lower concentration is known as the minority carrier. At equilibrium, the majority carrier concentration multiplied by the minority carrier concentration is always constant and is given by

$$n_o p_0 = n_i^2$$

where n_0 and p_0 are the equilibrium carrier concentrations of electrons and holes, respectively.

The majority and minority carrier concentrations can be written as:

For n-type; where $n_0 = N_D$, $p_0 = \frac{n_i^2}{N_D}$

For p-type; where $p_0 = N_A$, $p_0 = \frac{n_i^2}{N_A}$

where N_D is called the concentration of donor atoms and N_A is called the concentration of acceptor atoms. As the amount of doping increases, the number of minority carriers drops (C.B.Honsberg & S.G.Bowden, 2019).

1.4.2 Material Properties of Silicon

Si is the most often used material in photovoltaic cells. Because it is present in nature as silicon dioxide in sand and quartz, it accounts for 26% of the earth's crust. In solar cells, both crystalline and amorphous Si is employed. Because of the variances in the crystalline structure, there are differences in physical properties. (Green, 2015). Si has a bandgap of 1.12 eV, which shrinks as the temperature rises, shown in Figure 5.

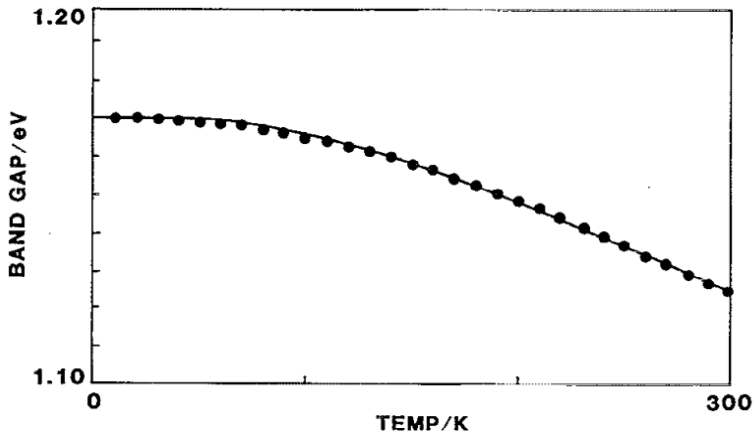

Figure 5. Silicon's energy bandgap as a function of temperature (O'Donnell & Chen, 1991).

A substance's conductivity is determined by dividing the current density by the applied electric field. Mobility may be shown as a function of the electric field since the charge of mobile carriers equals the current density. The following is the result of combining electrons and holes:

$$J = qnv_e + qpv_n = q(n\mu_n + p\mu_p)\varepsilon$$

The conductivity of electrons and holes is represented as follows:

$$\sigma = \frac{\Delta J}{\varepsilon} = q(n\mu_n + p\mu_p)$$

Because the conductivity is the inverse of the resistivity;

$$\rho = \frac{1}{\sigma} = \frac{1}{q(\mu_n n + \mu_p p)}$$

1.4.3 Carrier Generation & Light Absorption

The absorption of light and the formation of an electron-hole pair are required for the operation of a solar cell. Photons that reach the surface of a semiconductor are reflected, absorbed, or transmitted through the material. Reflection and transmission are considered loss mechanisms for photovoltaic systems since photons that are not absorbed do not generate power. If a photon is absorbed, it can excite an electron from the VB to the CB. The energy of a photon can be used to determine whether it is absorbed or transmitted. Therefore, a photon with enough energy will excite the electron to the CB. Photons that are falling onto a semiconductor material can be explained as follows compared to their energy and the semiconductor's bandgap:

- $E_{ph} < E_G$ has only a weak interaction with the semiconductor, flowing through it as if it were transparent.
- $E_{ph} = E_G$ absorbs well and has exactly the right amount of energy to produce an electron-hole pair.
- $E_{ph} > E_G$ strongly absorbed. The photon energy is higher than the bandgap. On the other hand, it will be wasted in photovoltaic applications because the electrons will quickly heat back to the CB.

Both majority and minority carriers are created by photon absorption. The quantity of light-generated carriers, on the other hand, is smaller than the amount of majority carriers in the semiconductor. Therefore, the majority carrier concentration does not change significantly with light. For the case of minority carriers, the number of light-generated minority carriers outweighs the number of existing minority carriers in the

semiconductor in the dark. The number of light-generated carriers can approximate the number of minority carriers in an illuminated semiconductor.

The absorption coefficient describes how far a specific wavelength of material light can reach before being absorbed. Low-absorption-coefficient materials absorb light weakly, and if the material is thin enough, it can act as a transparent to the wavelength in question. As a result, both the material and the wavelength of light absorbed impact the absorption coefficient. The energy of light is inadequate to move an electron from the VB to the CB below the bandgap. This light does not absorb as a result. As a result, the absorption coefficient of a semiconductor has a sharp edge.

The absorption of photons with energies close to the bandgap energy will be limited because electrons at the edge of the valence band can interact with photons and induce absorption. Electrons with energy close to the bandgap can interact with the increased photon energy, but if there are many electrons, this event may cause absorption.

By the following formula, the absorption coefficient α is dependent on the extinction coefficient, k:

$$\alpha = \frac{4\pi k}{\lambda}$$

where λ is the wavelength.

This connection demonstrates that different wavelengths penetrate a semiconductor at various distances. The absorption depth is the inverse of the absorption coefficient and is written as α^{-1}.

Absorption depth is a valuable metric, which means that the distance of light intensity inside the material is reduced by 1/e or about 36% of the original value. Owing to its high absorption coefficient, high-energy light (short wavelength) absorbs quickly, while low-energy light (long wavelength) absorbs slowly. As a result, not all of the red light is absorbed by the Si after a few hundred microns. The number of electrons generated at each point in the device due to photon absorption

is known as the generation rate. Consequently, generation is an essential factor in the operation of solar cells.

Its absorption coefficient and thickness determine the amount of light absorbed by a substance without considering reflection. The following equation can be used to measure the intensity of light at any point on the device:

$$I = I_0 e^{-\alpha x}$$

where I_0 is the light intensity at the surface, x is the distance, and α is the absorption coefficient.

The equation above may be used to compute the number of electron-hole pairs produced in a solar cell. The generation of an electron-hole pair in a tiny slice of material can be determined by integrating the light intensity over the narrow slice if light intensity is lost. Consequently:

$$G = \alpha N_0 e^{-\alpha x}$$

where N_0 is the photon flux at the surface and x is the distance into the material.

Light intensity drops rapidly within the material, as shown by the previous equation, and generation is highest near the material's surface.

The generation rate at each wavelength varies due to the vast range of wavelengths in the incident light, as shown in Figure 6. The rate of generation in Si, for example, can be shown below at various wavelengths. (C.B.Honsberg & S.G.Bowden, 2019).

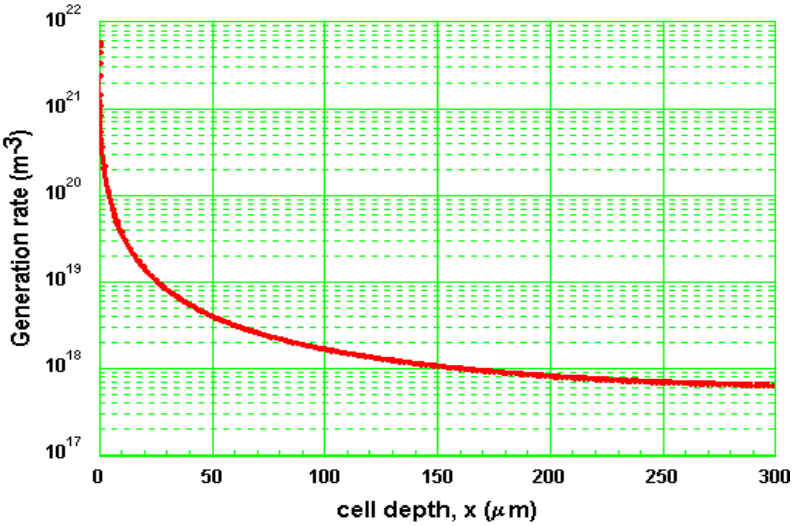

Figure 6. Generation rate of electron-hole pairs in silicon as a function of distance into the cell (C.B.Honsberg & S.G.Bowden, 2019).

1.4.4 Recombination

The energy released when an electron recombines with a hole is either heat or light, the polar opposite of generation. The Radiant recombination, Auger recombination, trap assisted recombination, and surface recombination are the four forms of recombination that occur in the bulk of a single-crystal semiconductor shown in Figure 7.

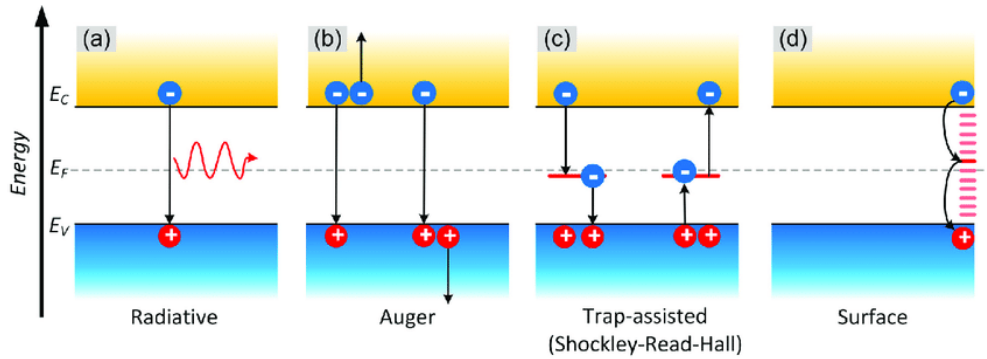

Figure 7. Recombination types (Plakhotnyuk, 2018).

In the indirect bandgap semiconductors, the recombination mechanism is dominated by non-radiative recombination. The radiative recombination in a semiconductor

device can be seen in the light emitted by a light-emitting diode (LED). Si, an indirect bandgap semiconductor with a very low radiative recombination, is used in most terrestrial solar cells.

Trap-assisted recombination, also known as Shockley-Read-Hall (SRH or RHS) recombination, occurs in the bandgap and is aided by a trap level of defect energy. *Defect recombination* is a two-step process in which an electron (or hole) is held in the forbidden region by an energy state caused by defects in the crystal lattice. These defects may be inherent to the material, or they may be introduced deliberately, for example, through doping. Second, a hole recombines if heated to the same energy level as an electron before thermally re-emitting. The energy level near the intermediate gap is sufficient for recombination because recombination is unlikely to occur near the valence or CB boundary.

In auger recombination, three carriers are engaged. Under concentrated sunlight at high carrier concentrations, heavy doping or high-level injection causes an electron and a hole to recombine, and the energy is transferred to another electron in the CB, which thermalizes back to the CB edge. When a material is heavily doped, the lifetime of Auger recombination is shortened. Auger recombination, for example, is a limiting factor for the lifetime and ultimate efficiency of Si-based solar cells.

Defects or impurities cause recombination on the surface or in the semiconductor. Because it reflects a severe disturbance of the crystal lattice, the solar cell surface is an area of high extreme recombination -this region of minority carriers is reduced by the high recombination rate at the top of the surface-. A limited region of low carrier concentration, on the other hand, causes carriers from higher concentration regions to flow into this location. As a result, minority carriers moving toward the surface restrict the rate of surface recombination. Surface recombination velocity is a parameter that describes recombination at a surface. The carriers' travel to the surface is zero when there is no recombination in a surface, which indicates the surface recombination velocity is zero. The highest velocity at maximum recombination hence limits carrier movement to the surface. Dangling bonds occur on the surface of the semiconductor when the periodicity of the crystal lattice is perturbed. Surface

recombination can be decreased by tying up those dangling bonds with an extra growing layer on top of the semiconductor surface. Surface passivation is the term for the process of reducing dangling bonds.

Assume that any external stimulation, such as the incident sun, causes minority carriers to rise over the equilibrium level. The surplus minority carriers will drift back to that equilibrium carrier concentration as a result of and through the recombination process. In a solar cell, the recombination rate, based on surplus minority carriers, is thus a significant parameter. The recombination rate is 0 when there are no extra minority carriers. Minority carrier lifetime and diffusion length are thus two essential recombination rate parameters.

The average duration before a carrier recombines how much time it spends in an excited state after generation, given by n or p, is referred to as the minority carrier lifetime of material. The lifetime of low-level injected material is linked to the recombination rate.

$$\tau = \frac{\Delta n}{R}$$

where τ is the minority carrier lifetime, Δn is the excess minority carriers' concentration, and R is the recombination rate.

$$\frac{1}{\tau_{bulk}} = \frac{1}{\tau_{band}} \frac{1}{\tau_{Auger}} \frac{1}{\tau_{SRH}}$$

The lifetime of Auger is calculated as a function of carrier concentration:

$$\tau_{Auger} = \frac{1}{CN_A^2}$$

where the auger coefficient, C, for Si is $1.66 \times 10^{-30} cm^6/s$.

Another significant metric is the minority carrier diffusion length, which is related to the collection probability and represents the average distance a carrier may travel from generation to recombination. The diffusion length is equal to the carrier lifetime multiplied by the diffusivity.

$$L = \sqrt{D\tau}$$

where L is the diffusion length, D denotes the diffusivity, and τ denotes the lifetime.

Recombination is caused by impurities or defects inside or on the surface of the semiconductor. The solar cell surface has a very high recombination rate because it represents a significant disturbance of the crystal lattice. High recombination rates at the surface deplete the region of minority carriers, whose rate toward the surface is the rate-limiting factor for surface recombination. The flow of carriers toward the surface is zero when there is no recombination at the surface, and the surface recombination velocity is also zero. At indefinitely fast recombination, the carriers' maximum velocity limits their travel. When the periodicity of the semiconductor's crystal lattice is disrupted, defects appear on the surface, and dangling bonds form. Surface passivation, an extra layer on top of the semiconductor's surface, bonds these dangling bonds, lowering surface recombination. Limiting surface recombination resulted in extended cell lifetimes because the concentration of minority carriers determines the lifetime of the material. Surface recombination must be limited to prevent minority carrier depletion. Consequently, the material's lifetime can be extended (Hubbard, 2016).

1.4.5 P-n Junction and Carrier Transport

P-n junctions are formed by joining n-type and p-type semiconductor materials. The p-type part of the p-n junction has a high hole concentration, whereas the n-type area has a high electron concentration. Because there are more electrons in the n-type zone than holes, the electrons tend to diffuse to the p-type region. Similar to holes in the p-type zone, holes in the n-type region tend to diffuse. These carriers leave exposed charges behind when they migrate from one side to the other, and these charges become fixed in the crystal lattice. Positive ion cores are exposed charges in the n-type region, while negative ion cores are exposed in the p-type zone. As a

result, an electric field (E) arises between them, resulting in a depletion area. A built-in potential Vbi is created as a result of the electric field.

When there are no external inputs at the p-n junction, the electric field in the depletion area creates equilibrium between carrier generation, recombination, diffusion, and drift. Diffusion current refers to the movement of carriers across a junction.

The three modes of operation for semiconductor devices are thermal equilibrium, steady-state, and transient. There are no external inputs during thermal equilibrium. As a result, the device will have no net current since the currents will be balanced. There are external inputs like light or applied voltage in a steady-state, but the circumstances remain constant. Devices are generally operated in a steady state with either forward or reverse bias. Due to the rapidly fluctuating voltage, the solar cell responds with a slight delay.

The electric field at the junction is lowered when a forward bias is supplied, which refers to applying a voltage across the device. Because lowering the electric field disturbs equilibrium, the barrier to carrier diffusion is lowered, increasing the diffusion current. The drift current will remain constant as the diffusion current increases because the amount of carriers created in the depletion zone or within the region's diffusion length depends on the diffusion current. The number of minority carriers will not change significantly because the depletion region is only slightly reduced.

Due to increased diffusion from one side of the junction to the other, minor carrier injection may occur at the boundary of the depletion zone. Diffusion causes these carriers to travel away from the junction and finally reunite with a majority carrier. Under forward bias, most carriers are provided by an external circuit, thereby generating a net current. In the absence of recombination, the minority carrier concentration would reach a new, higher equilibrium concentration, and carrier diffusion from one side of the junction to the other would halt, similar to when two different gases are introduced. When a uniform concentration is reached, gas

molecules migrate in a net direction from the high carrier concentration region to the low carrier concentration region. Minority carriers introduced into a semiconductor, on the other hand, recombine, allowing more carriers to diffuse across the junction. As a result, the recombination current in the forward-biased diffusion current. The higher the rate of recombination events, the stronger the current flowing across the junction.

The dark saturation current (I_0) is a critical feature that separates one diode from the next. I_0 measures the recombination in the device. As a result, a diode with more recombination will have a higher I_0.

A voltage is applied across the device in reverse bias to boost the electric field at the junction. The probability of carriers diffusing from one side of the junction to the other reduces as the electric field in the depletion zone develops, and the current diffusion drops. The quantity of minority carriers on either side of the p-n junction limits the drift current, just as it does in advancing bias, and the higher electric field has little effect. A slight increase in the width of the depletion region causes a slight rise in the drift current in Si solar cells; still, this fact is a second-order effect. The change in depletion area width with voltage significantly impacts cell function in many thin-film solar cells, where the depletion zone is about half the thickness of the solar cell.

A voltage function that expresses current across a diode is the diode equation. The Ideal Diode Law is phrased as follows:

$$I = I_0(e^{\frac{qV}{kT}} - 1)$$

Where I is the diode's net current, I_0 is the dark saturation current, V is the applied voltage across the diode's terminals, q is the electron charge's absolute value, k is Boltzmann's constant, and T the is absolute temperature.

In the case of actual diodes, the expression is:

$$I = I_0(e^{\frac{qV}{nkT}} - 1)$$

where n is the ideality factor (a value between 1 and 2).

1.4.6 Solar Cell Structure

Solar cells are electrical devices that convert sunlight directly into energy. To create electric power, light shining on the solar cell generates both a current and a voltage. This procedure necessitates two things: first, a material in which light absorption elevates an electron's energy state, and second, the transfer of that higher energy electron from the solar cell to an external circuit. After dissipating its energy in the external circuit, the electron returns to the solar cell. Various materials and techniques might theoretically meet the requirements for photovoltaic energy conversion, but in reality, semiconductor materials in the form of a p-n junction are used in almost all photovoltaic energy conversion. In Figure 8, a cross-section of a primary solar cell can be seen.

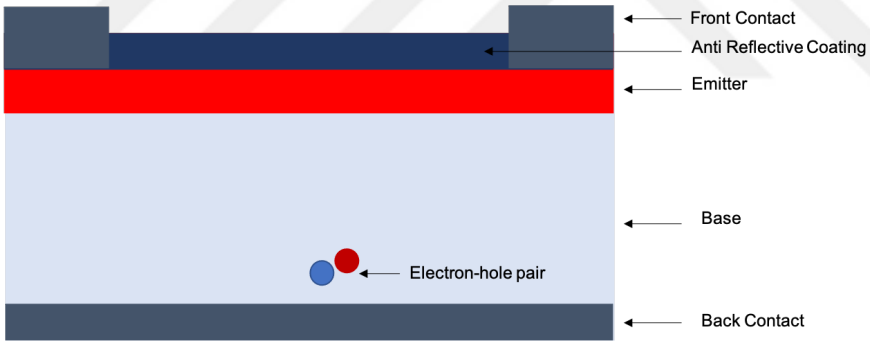

Figure 8. Cross section of a solar cell.

1.4.7 Solar Cell Parameters

The I-V curve of a solar cell is the superposition of the solar cell diode's IV curve in the dark with the current produced by light. The light causes the I-V curve to move down towards the fourth quadrant, allowing power to be extracted from the diode. When a cell is illuminated, it adds to the diode's typical "dark" currents, resulting in the following diode law:

$$I = I_0 \left[exp\left(\frac{qV}{nkT}\right) - 1 \right] - I_L$$

Where I_L is the light-generated current.

In Figure 9, the I-V curve of a solar cell can be seen.

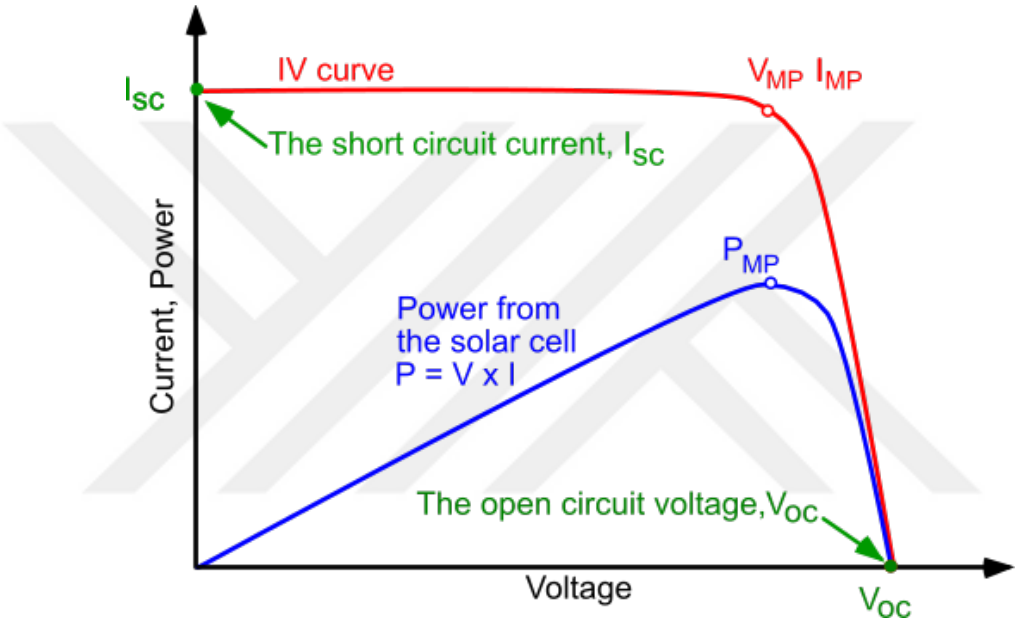

Figure 9. I-V curve of a solar cell.

In a more thorough examination, the I-V curve ranges between short circuit current (I_{SC}) and open-circuit voltage (V_{OC}), as shown in Figure 10. V_{OC} is the maximum voltage at zero current, while I_{SC} is the maximum current at zero voltage. At the maximum power point, which is positioned at the knee of the I-V curve, maximum electrical power may be produced. In addition, the inverse slope of the I-V curve at zero voltage and zero current points may be used to deduce information about R_s and R_{sh}.

Another solar cell parameter fill factor (FF) is the ratio of maximum power, which is the product of V_{mp} and I_{mp}, to V_{OC} and I_{SC}. FF is the measure of the squareness of

the I-V curve and can be calculated from the area of the largest rectangle fitting in the I-V curve.

$$FF = \frac{V_{mp}.I_{mp}}{V_{oc}.I_{sc}}$$

One electron flows in the external circuit when a photon strikes the cell with greater energy than the semiconductor's bandgap. Using the photon flux for each wavelength of incoming photons and integrating the energy distribution throughout the whole range, the maximum I_{SC} can be determined. Saturation current I_0 must be kept to a minimum for maximum V_{OC}. According to the saturation current equation, I_0 grows as the bandgap lowers, V_{OC} drops, and I_{SC} rises.

$$V_{oc} = \frac{nkT}{q} \ln\left(\frac{I_L}{I_0} + 1\right)$$

$$I_0 = 1.5\ x\ 10^5 \exp\left(-\frac{E_g}{kT}\right)$$

The most often used solar cell metric is energy conversion efficiency (η), which is defined as the ratio of power that can be transferred from incident sunlight via solar cell to the incident light power density and is expressed as;

$$\eta = \frac{FF.V_{oc}.I_{sc}}{P_{in}} = \frac{P_{mp}}{P_{in}}$$

where P_{in} is the total power of the light incident of the cell.

CHAPTER 2

THEORY

2.1 Contacts and Contact Resistivity

A significant mismatch between the Fermi energy of the metal and the semiconductor might result in a high-resistance rectifying contact. On the other hand, a good material selection can result in a low resistance ohmic contact. Most metal-semiconductor contacts are annealed or alloyed after metal deposition to improve contact resistance.

2.1.1 Schottky-Mott Theory

The presence of an electric barrier between the metal and the semiconductor allows a metal-semiconductor to contact to be rectified. The differing work functions of the two materials generate this barrier. If the metal's work function (ϕ_m) is greater than the semiconductor's (ϕ_s), to balance the Fermi levels, electrons move from the semiconductor to the metal, leaving a depletion area in the semiconductor with the bands bent upwards (Figure 11 (a) for an n-type semiconductor). According to Gauss' theory, the electric field intensity will rise linearly with distance from the depletion zone's edge as the metal approaches if space charges are evenly distributed throughout the depletion region. A Schottky barrier, also known as a parabolic potential barrier, is formed when the electrostatic potential increases quadratically. For example, a simple argument may prove that the degree by which the bands are bent upwards, known as the diffusion potential V_{do}, is given by,

$$V_{do} = \emptyset_m - \emptyset_s$$

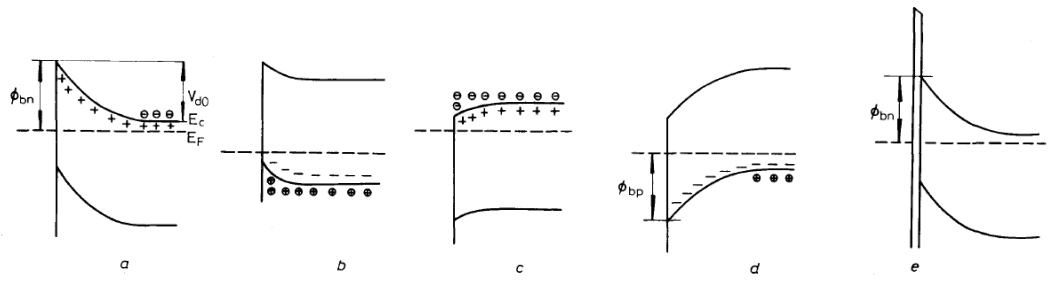

Figure 10. Schottky barriers for semiconductors of various kinds and work functions (a) $\phi_m > \phi_s$ for n-type, (b) $\phi_m > \phi_s$ for p-type, (c) $\phi_m < \phi_s$ for n-type, (d) $\phi_m < \phi_s$ for p-type and (e) $\phi_m > \phi_s$ for n-type with an interfacial layer (Rhoderick, 1982).

The energy of an electron owing to its electrostatic potential is equal to the magnitude of the potential expressed in volts since all energies are measured in electron volts. If $\phi_m > \phi_s$, V_{do} is positive, and the bands are bent upwards; this creates a barrier that electrons to pass through in order to flow from the semiconductor to the metal, as illustrated in Figure 10 (a), resulting in rectifying characteristics. The band-bending has no influence on the mobility of the holes in a p-type semiconductor ((Figure 10 (b), and no rectification occurs, resulting in an ohmic contact. If $\phi_m<\phi_s$, the bands are bent downwards, resulting in ohmic contact for an n-type semiconductor (Figure 10 (c)) and a rectifying contact for a p-type semiconductor (Figure 10 (d)) due to the difficulty of passing holes under a barrier. Because $\phi_m > \phi_s$ for n-type semiconductors and $\phi_m < \phi_s$ for p-type semiconductors in nearly all situations, most metal-semiconductor pairings create rectifying contacts.

The barrier height ϕ_b, as seen from the metal, is typically provided rather than the diffusion potential. For an n-type semiconductor, this is given by

$$\phi_{bn} = V_{do} + (E_C - E_V) = \phi_m - \chi_S$$

where χ_s $\{=\phi_m-(E_C-E_F)\}$ is the semiconductor's electron affinity, in other words, the difference between the vacuum level and CB energies.

It is obtained by assuming that when the metal and semiconductor come into contact, the surface dipole contributions to ϕ_m and χ_s do not change.

The ideal condition illustrated in Figure 10 (a) is seldom attained because most metal-semiconductor contacts have a tiny oxide layer on the surface of the semiconductor, around 1-2nm thick. An interfacial layer is the name given to this sort of oxide film. As a result, a successful contact resembles Figure 10 (e). However, because the oxide layer's extra barrier is generally so tiny that electrons may readily travel through it via quantum-mechanical tunneling, the electrical characteristics of Figure 10 (a) and (b) are nearly identical (e).

When the semiconductor and the metal are brought into contact, the Schottky-Mott approximation assumes that the surface dipole contributions to ϕ_m and χ_s do not change. The electron cloud of the surface atoms is distorted, causing the centers of the positive and negative charge distributions to not coincide, since the atoms at the solid surface only have neighbors on one side. However, it was quickly observed that the linear dependency of ϕ_{bn} on ϕ_m anticipated by $\phi_{bn}=\phi_m-\chi_s$ does not occur in practice, and therefore the assumption of surface dipole layer constancy cannot be trusted.

The atoms only have neighbors on one side of the surface, while the valence electrons have no partners to establish covalent connections on the vacuum side. As a result, each atom on the surface has an unpaired electron in a restricted orbital pointing away from it. A dangling bond refers to an orbital with a dangling bond. It can either give or take an electron, therefore it may act as a donor or acceptor. Within the prohibited gap, the surface states have a very uniform energy distribution. and are defined by a neutral level ϕ_0 such that the surface is electrically neutral if the surface states are populated up to ϕ_0 and vacant above ϕ_0. The surface states will have a net charge in this case because the Fermi level does not always coincide with the neutral level. The charge in the surface states, combined with its image charge on the metal's surface, will create a dipole layer if a thin oxide layer exists between the metal and the semiconductor, as is the case if the latter's surface has been chemically polished. The potential difference between the semiconductor and the metal will be altered by this dipole layer.

According to the Bardeen model, the barrier height is about equivalent to

$$\phi_{bn} = \gamma(\phi_m - \chi_s) + (1-\gamma)(E_g - \phi_0) \; where \; \gamma = \epsilon_i/(\epsilon_i + q\delta D_s)$$

The semiconductor bandgap is E_g, the oxide layer thickness is δ, and the total permittivity is ϵ_i. Within the bandgap, the surface states are considered evenly distributed in energy, with a density D_s per electron-volt per unit area. The neutral level ϕ_0 is located at the top of the valence band and is measured from there.

In the case of a p-type semiconductor, ϕ_{bp} is roughly given by

$$\phi_{bp} = \gamma(E_g - \phi_m + \chi_s) + (1-\gamma)\phi_0$$

2.1.2 Ohmic Contacts

A metal-semiconductor junction produces an Ohmic contact if the Schottky barrier height (f_B) is negative or zero. As there will be negligible resistance at the contact, the carriers will be free to flow in and out of the semiconductor. The metal's electron affinity must be close to or larger

than the work function of an n-type semiconductor. In a p-type semiconductor, the metal's work function must be greater than or equal to the sum of the electron affinity and bandgap energy.

2.1.2.1 Tunnel Contacts

Tunnel contacts have a positive barrier at the metal-semiconductor interface, and because the semiconductor is sufficiently doped, there is only a thin barrier between the metal and the semiconductor. Carriers easily tunnel over such barriers because the depletion area at the metal-semiconductor interface is narrow. The necessary doping density for such contact should be equal to or more than 10^{19} cm^{-3}.

2.1.2.2 Annealed or Alloyed Contacts

Metals must be deposited at a high temperature for the production of Ohmic contacts. Because metal alloys containing semiconductors and high-temperature annealing lower the unintended barrier at the interface, this step is required.

2.1.3 Contact Resistance to a Thin Semiconductor Layer

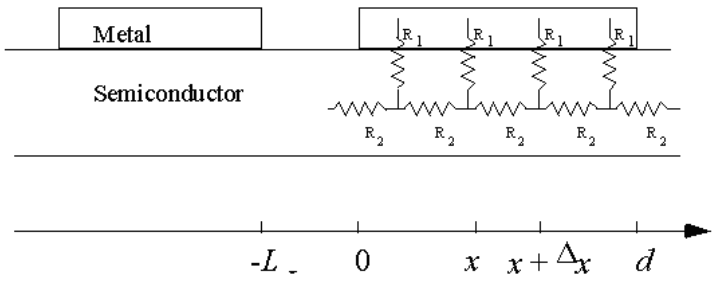

Figure 11. A contact to a thin semiconductor layer with a distributed resistance model (Zeghbroeck, 2010).

The equivalent circuit represented in Figure 11 is produced by slicing the structure into D_x; so, the contact resistance (R_1) and the semiconductor resistance (R_2) may be represented as:

$$R_1 = \frac{\rho_C}{W\Delta x} \quad and \; R_2 = R_s \frac{\Delta x}{W}$$

Where ρ_c is the metal-to-semiconductor interface contact resistance per unit area, R_s is the semiconductor layer's sheet resistance, and W is the contact width.

The following are the relationships between voltage across the metal-semiconductor interface and current obtained using Kirchhoff's rules (x), parallel to the interface at x and x+Δx

$$V(x+\Delta x)-V(x)=I(x)R_2=I(x)\frac{R_S}{W}\Delta x \quad I(x+\Delta x)-I(x)=\frac{V(x)}{R_1}=V(x)\frac{W}{\rho_c}\Delta x$$

The differential equations for I(x) and V(x) may be found by allowing D_x approach zero:

$$\frac{dV}{dx}=\frac{I(x)R_s}{W} \qquad \frac{dI}{dx}=\frac{V(x)W}{\rho_C}$$

These equations can be combined to form the following:

$$\frac{d^2I(x)}{dx^2}=I(x)\frac{R_s}{\rho_c}=\frac{I(x)}{\lambda^2} \quad with\ \lambda=\sqrt{\frac{\rho_c}{R_s}}$$

The penetration length, defined as the typical distance across current variations beneath the metal contact, is the parameter λ. As a result, the general solution for I(x) and V(x) is as follows:

$$I(x)=I_0\frac{sinh\frac{d-x}{\lambda}}{sinh\frac{d}{\lambda}} \qquad V(x)=I_0\frac{\lambda R_s}{W}\frac{cosh\frac{d-x}{\lambda}}{sinh\frac{d}{\lambda}}$$

The total resistance of the contact is;

$$R_c=\frac{V(0)}{I(0)}=\frac{\lambda R_s}{W}cot\frac{d}{\lambda}=\frac{\sqrt{\rho_c R_s}}{W}cot\frac{d}{\lambda}$$

For the case of infinitely long contact (d >> l), the contact resistance is given by;

$$R_c=\frac{\sqrt{\rho_c R_s}}{W}, for\ d\gg\lambda$$

A measurement of the resistance between the contacts with distance L, which is referred to as a TLM structure, can therefore be expressed as;

$$R=2\frac{\sqrt{\rho_c R_s}}{W}+R_s\frac{L}{W}$$

so that the resistance per square, R_s, can be obtained from the slope, while the contact resistivity, ρ_c, can be obtained from the intersection with the y-axis. The penetration depth, l,

can be obtained from the intersection with the x-axis. In Figure 12, resistance versus the contact spacing can be seen.

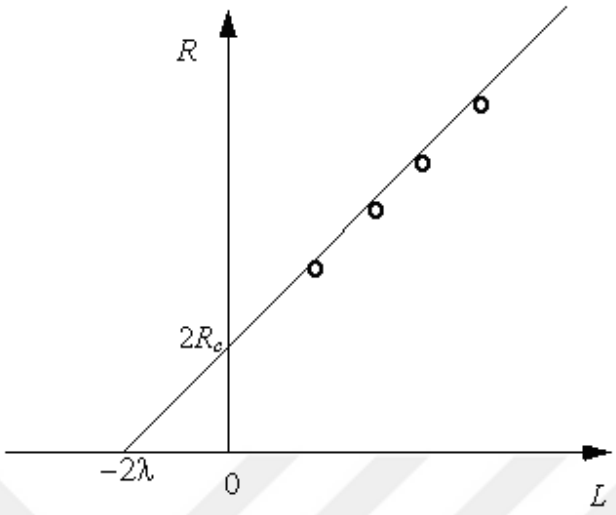

Figure 12. Resistance versus contact spacing, L, of a transmission line structure (Zeghbroeck, 2010).

In the limit for short contact (or d << l), the contact resistance can be approximated by expanding the hyperbolic cotangent:

$$R_c = \frac{\lambda R_s}{W}\left(\frac{\lambda}{d} + \frac{d}{3\lambda} + \cdots\right) = \frac{\rho_c}{Wd} + \frac{1}{3}R_s\frac{d}{W}, for\ d \ll \lambda$$

2.1.4 Contact Resistance and Contact Resistivity

It is not a useful point of comparison since contact resistance varies with contact size. So instead, we can use ρ_C.

Consider a small area at the contact's top, as seen in Figure 13.

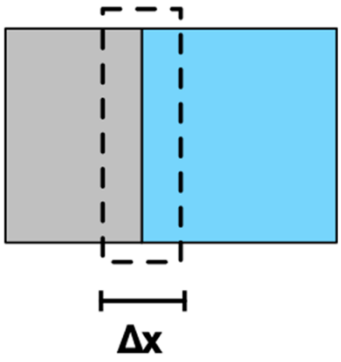

Figure 13. A small region at the top of the contact.

$$R_C = \rho' \frac{\Delta x}{A_C}$$

where A_C is the area of the contact.

$$\rho_C = \lim_{\Delta x \to 0} (\rho' \Delta x) = R_C A_C$$

The current flow through the semiconductor is uniform, but it is not uniform in the contacts. We can't use the physical length and breadth of the contact to calculate the contact area since the current flow isn't uniform in the contact. At the contact's edge, the current flowing in and out is considerable. Current crowding occurs when the current drops off from that edge until there is no current at the far edge. Current crowding shows the drops off exponentially with a characteristic length of L_T, known as the transfer length, which can be considered the contact's effective length, shown in Figure 14.

$$L_T = \sqrt{\frac{\rho_C}{R_C}}$$

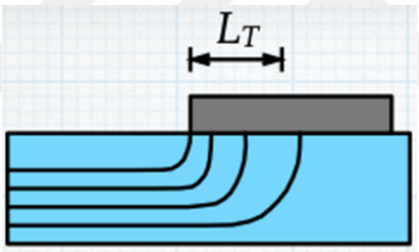

Figure 14. Transfer Length.

The transfer length is the average distance traveled by an electron or a hole in the semiconductor under the contact before it flows into the contact. So, the effective area of the contact is defined as $L_T W$.

So,

$$R_C = \frac{\rho_C}{L_T W} = \frac{R_S L_T}{W} \; and \; R_T = R_{semi} 2R_C = R_S \frac{L}{W} + 2\frac{R_S L_T}{W} = \frac{R_S}{W}(L + 2L_T)$$

The plot of R_T vs. L_T can also transfer length by extrapolating back to the horizontal axis, where the intercept is equal to $-2L_T$.

2.2 Characterization Techniques

2.2.1 Four-Point Probe

A four-point probe shown in Figure 15 is for measuring the resistivity of semiconductor samples. Two exterior probes are used to pass current, while the inside probes are used to detect voltage, allowing the substrate resistivity to be measured. Additionally, resistivity may be used to compute doping concentration.

The sheet resistivity of the top emitter layer may be readily tested with a four-point probe. A voltage is produced in the inner voltage probes by a current flowing through the exterior probes. The barrier between the n and p-type materials is the insulating layer. As a result, the cell must be kept dark during the measurement.

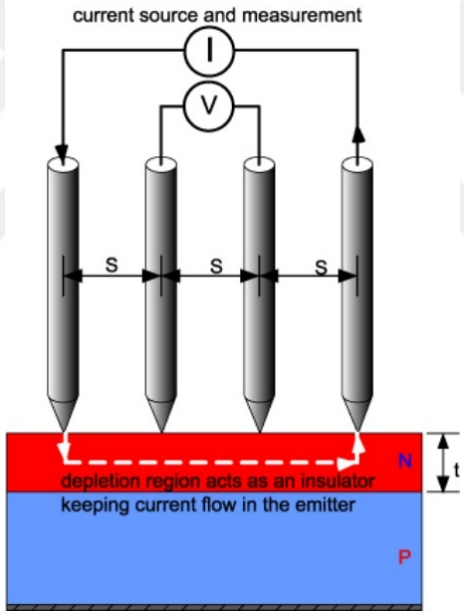

Figure 15. Four-point probe schematic (C.B.Honsberg & S.G.Bowden, 2019).

Using the probe's voltage and current readings:

$$\rho_{\square}\left(\frac{\Omega}{\square}\right) = \frac{\pi}{\ln(2)}\frac{V}{I} \; where \; \frac{\pi}{\ln(2)} = 4.532$$

Si solar cells' emitter sheet resistivity is typically between 30-100 Ω/□.

Bulk resistivity is measured in the same way as sheet resistivity.

$$\rho_{\square}\left(\frac{\Omega}{\square}\right) = \frac{\pi}{\ln(2)}\frac{V}{I}t = 4.532\left(\frac{V}{I}\right)t \quad where\ t\ is\ the\ wafer\ thickness\ in\ cm$$

This formula works when the wafer thickness is less than half the probe spacing (t<s/2) 2. For thicker samples, the formula becomes:

$$\rho = \frac{V}{I} = \frac{\pi t}{ln\left(\frac{sinh\left(\frac{t}{s}\right)}{sinh\left(\frac{t}{2s}\right)}\right)} \quad where\ s\ is\ the\ probe\ spacing.$$

Because the connections to the Si are ohmic, low resistivity samples are generally considerably easier to analyze. Furthermore, for samples with low resistivity, the current flowing through the sample causes resistive heating, which raises the measured resistivity.

The current is decreased for high resistivity samples to avoid having an abnormally higher voltage at the contacts. It is suggested that the internal probes have a voltage of less than 100 mV/mm.

2.2.2 Electrochemical Capacitance-Voltage Measurement

Electrochemical capacitance-voltage (ECV) profiling is used to measure doping profiles in semiconductor layers through a depth-dependent CV measurement by altering the conditions at the semiconductor/electrolyte interface and controlling the etching of the material. In order to create a depletion region, the technique uses an electrolyte-semiconductor Schottky contact which contains ionized donors and electrically active traps or defects. The created depletion region behaves like a capacitor with its ionized charges inside. The measurement of the capacitance provides information on the doping and electrically active dopant densities. With electrolytically etching, depth profiling is achieved with capacitance measurements and no depth limitation between the semiconductors. The equipment schematic can be seen from in Figure 16.

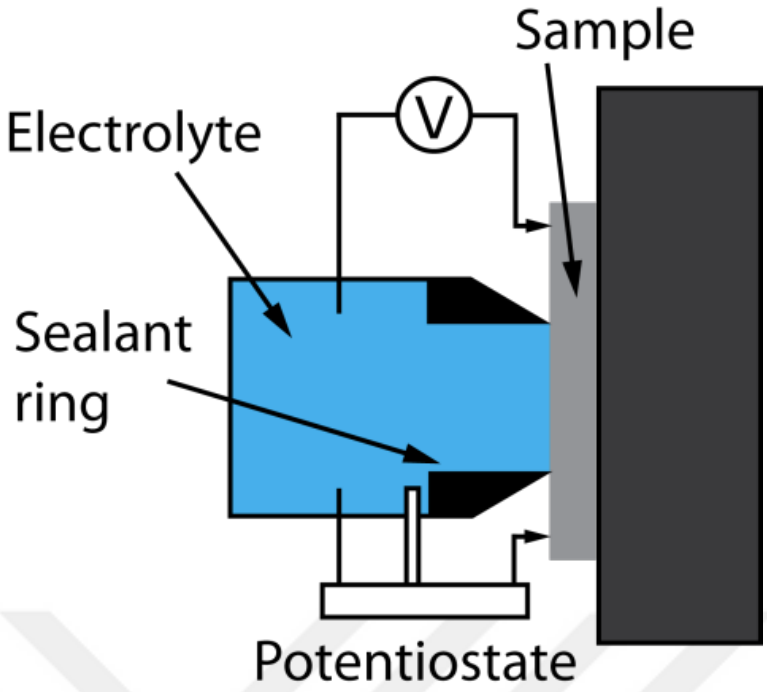

Figure 16. Electrochemical capacitance-voltage measurement equipment schematic (Electrochemical CV-Profiling, n.d.).

A sealing ring is pushed against the sample in an electrochemical cell containing an electrolyte. The ring-opening is the contact area, and the depletion region is created by applying a potential between the semiconductor and the electrode measured for reference. Between the semiconductor and the counter electrode, there is a current circuit that regulates the etching conditions. Carriers will be attracted or repelled depending on the charge of the ions in the solution adjacent to the interface in the field-affected region. In order to measure the carrier concentration by CV methods, conditions must be such that a region depleted of carriers is formed. For a p-type semiconductor, where the majority of carriers are holes, this condition is satisfied by positive ions in the solution. Positive ions are attracted to the interface when the semiconductor is made more negative than its equilibrium value, whereas holes are repelled. Negative ions are necessary for an n-type semiconductor with electrons as the majority carrier; hence the semiconductor must be made to have a positive value that is greater than its equilibrium value.

When the dissolution process is taken into account, the advantages of utilizing an electrolyte become apparent. Depth profiling is accomplished by electrolytically dissolving the semiconductor; the dissolution process causes an increase in the separation of electric charge, which is dependent on holes. The majority of carriers in p-type semiconductors are holes, and dissolution is easily accomplished by forward biasing the electrolyte-semiconductor junction.

From the valence to the CB, electrons are excited by light with a short enough wavelength, leaving holes behind that are drawn to the surface by reverse biasing the junction (*Electrochemical CV-Profiling*, n.d.).

2.2.3 Transmission Line Measurement (TLM)

The classic TLM test structure consists of parallel contact fingers with equal width but varying distances on a thin conducting layer, as shown in Figure 17. This means that the conducting sheet is much thinner than the smallest distance between the fingers.

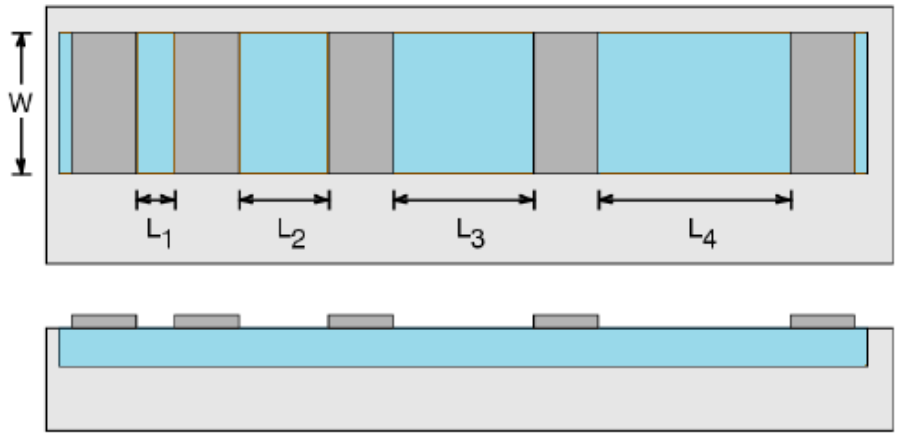

Figure 17. TLM pattern.

It is assumed that the sheet resistance is homogeneous and that the contact resistance is equal for each finger. The resistance between two neighboring fingers, for example 1 and 2, is then

$$R_{1,2} = 2R_C + R_{semi}\frac{L_1}{W}$$

A linear regression of the measured resistances vs. distances gives R_{sheet} from the slope and R_C from the axis intercept, as shown in Figure 18.

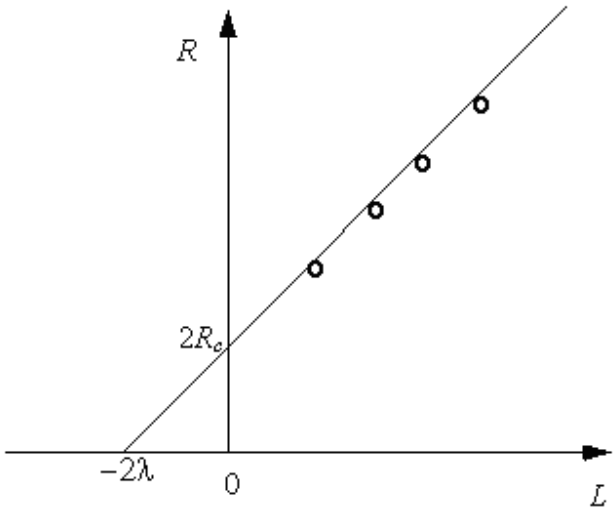

Figure 18. Resistance versus contact spacing, L, of a transmission line structure (Zeghbroeck, 2010).

The contact resistivity is calculated numerically, solving the following equation with Newton's method.

$$R_C = \frac{\rho_C}{W L_T} \coth \frac{W_F}{L_T}$$

where WF is the finger width and where the transfer length $L_T = \sqrt{\rho_C / R_{sheet}}$

In the measurements of this thesis, we used constant contact spacing. So, the resistance became with n number of intermediate fingers;

$$R = 2R_C + \frac{R_{sheet}}{W}\left[(n+1)L + n d_{eff}\right]$$

where d_{eff} is the effective width, which equals; $d_{eff} = 2L_T \tanh \frac{W_F}{2L_T}$. The value for d_{eff} ranges between W_F when the contact resistivity is very large and $2L_T$ if the contact resistivity is very low.

The sheet resistance is determined from the slope of a graph where the measured resistance is plotted vs. the distances (n + 1) L + n d_{eff}. In the first iteration, a value $d_{eff} = W_F$ is assumed. The contact resistance R_C is assumed to be equal for all fingers. It is determined again from the intercept at a distance equal to zero.

2.2.4 Concept of This Thesis

Ion implantation is an attractive doping method since it eliminates some standard and advanced cell fabrication (Hieslmair et al., 2012). Surface passivation of the p++ region is typically provided with Al_2O_3/SiN_x stack layer. In the metallization step of solar cell process flow, screen printing is commonly utilized for metal contact to the emitter. The ρ_C between metal and the underlying Si substrate depends on emitter doping concentration in the Si wafer and metal types used in the metallization process. Because of its high impact on the solar cell performance, the minimization of the ρ_C in the metalized area is a significant concern (Recart et al., 2007). For a particular type of paste and firing condition, the emitter doping level is generally inversely related to the ρ_C (Rane et al., 2003). It has been shown that front metal ρ_C decreases as the active dopant increases (Uddin, 2019). Except in rare circumstances, such as short activation time and low-temperature annealing or lengthy activation time and high-temperature annealing, the boron implanted emitter follows this pattern.

CHAPTER 3

EXPERIMENTAL METHODS

3.1 Ion Implantation and Dopant Activation

Ion implantation is a low-temperature, vacuum method that drives ions of an element into a target, modifying the target's physical, chemical, or electrical properties. At high speeds, ions clash with the target, creating chemical and physical changes. Because of the high energy, energetic collision cascades can disrupt the target's crystal structure, and ions with enough energy can trigger nuclear transmutation. The schematic of the ion implanter can be seen in Figure 19.

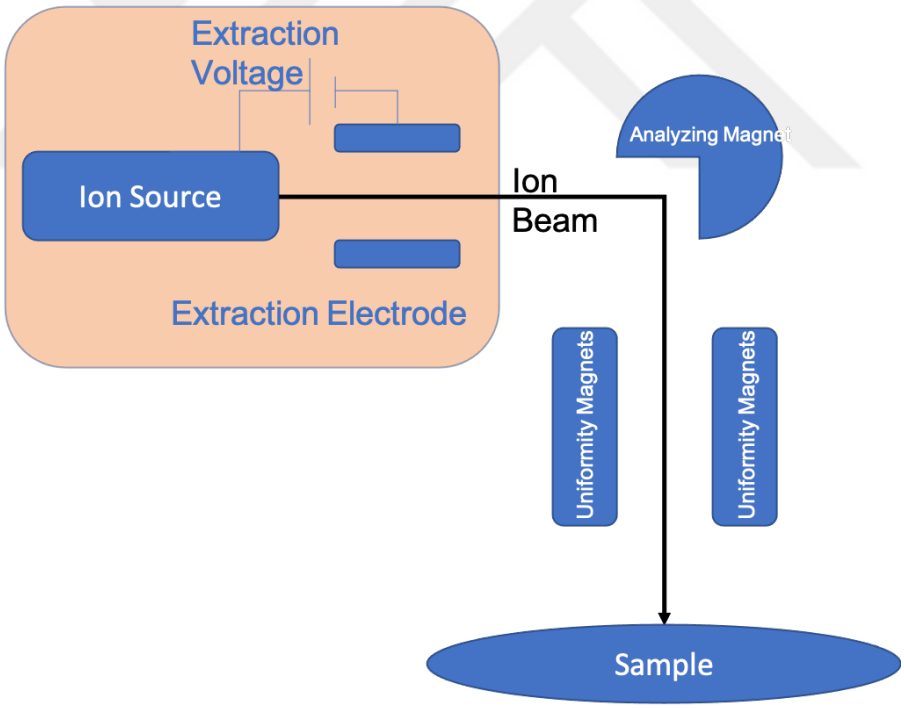

Figure 19. Ion Implanter schematic.

An ion source, an accelerator, and a target chamber are the most common components of ion implantation equipment. The ion source produces the desired

element, while the accelerator accelerates the ions electrostatically. Ions impinge on the target in the target chamber, and the implantation process begins. Because each ion is usually an atom or a molecule, the amount of implanted material may be determined using the integral of the ion current over time, known as dose.

The implantation's typical ion energies vary from 10 to 500 keV. Energies ranging from 1 to 10 keV are used to achieve implant depths of a few nanometers or less. Higher energies cause severe structural damage to the target, and because the Bragg peak causes a broad depth distribution, the composition change in the target at any site will be modest.

The ion species, target composition, and ion energy are all determined by the penetration depth. As a result of the monoenergetic ion beam, a broad depth distribution is produced. The penetration depth is typically between 10 nanometers and 1 micrometer. Because the ions progressively lose energy as they travel through the material and occasionally collide with target atoms, ion implantation is useful when chemical or structural change is required near the target's surface. The binary collision approximation method can promote the loss of ion energy, which causes stopping.

As the localized amorphous regions expand and overlap, ion implantation on Si generates crystal defects, localized amorphous material zones inside its seemingly crystalline structure, and continuous amorphous layers. Crystal defects and the development of amorphous material are both examples of primary crystalline damage. The ion-implanted substrate must be exposed to annealing, a reparative heating method, in order to be restored to its pre-implant condition.

Electrical activation of implanted impurities, initial crystalline damage annealing, annealing of continuous amorphous layers, dynamic annealing, and diffusion of implanted impurities are the five fundamental components of ion implantation damage annealing. It is carried out in a neutral atmosphere, such as Ar or N_2.

During annealing, electrical activation of newly implanted impurity atoms enhances their electrical activity, which generally does not occupy substitutional locations after being implanted. To eliminate trapping defects, the temperature is raised to 500 ^{o}C, releasing carriers to the process's VB or CB. At 500-600 ^{o}C, the formation of dislocations causes the electrical activity to decline again. After then, however, electrical activity rises until it reaches a peak temperature of 800-1000 ^{o}C.

Primary crystalline damage annealing involves the recombination of vacancies and self-interstitials at low temperatures (up to 500 ^{o}C), the formation of impurity-capturing dislocations at 500-600 ^{o}C, and the dissolution of these dislocations at 900-1000 ^{o}C. Between 500 and 600 ^{o}C, solid-phase epitaxy has been demonstrated to anneal the continuous amorphous layers extending to the surface. The amorphous layers begin to recrystallize beneath the crystalline substrate, with regrowth moving toward the substrate surface. Two variables impact the rate of recrystallization: crystal orientation and implanted impurities. Solid-phase epitaxy occurs at both amorphous-single crystal interfaces and regrowth contacts meeting below the surface, and amorphous layers do not extend to the surface anneal differently.

The repair of implant damage while the implantation procedure is still in progress is referred to as dynamic annealing effects. Because the heat given to the wafer during implantation makes the point defects more mobile, the dynamic annealing effect occurs.

Diffusion of implanted impurities refers to the mass movement of implanted species along a concentration gradient inside an implanted layer during the annealing process. Implant damage slows the diffusion process as compared to a single-crystal substrate that has not been damaged. If thermal processing is not finished quickly enough, diffusion of implanted contaminants during annealing can damage devices with shallow junctions or small base and emitter regions.

3.2 Passivation of the Surface

Surface passivation in Si solar cells inhibits premature recombination of electrons and holes on the wafer surface. For more than ten years, many deposition processes and materials have been used in the development process.

Trimethylaluminum (TMA) vapor reacts with oxygen to form the aluminum oxide passivation layer. TMA vapor reacts with oxygen at the substrate's surface, forming a thin aluminum oxide layer.

Al_2O_3 is a great passivation layer for boron emitters since stable passivation can be achieved rather than SiO_2 since it degrades under UV illumination because of the increase in defect density on the surface of Si/SiO_2. Furthermore, since Al_2O_3 is based on the electrical shielding of electrons by the vast amount of fixed negative charges, degradation under UV illumination is weaker than SiO_2 (Schmidt et al., 2008).

3.3 Anti-Reflective Coating (ARC)

A solar cell's ARC aids in increasing the amount of light absorbed into the cell. Because the reflection of bare Si solar cells is about 30%, this ARC is required. Silicon nitride or titanium oxide is used for the thin AR Coating.

Due to its capacity to perform several roles while obviating the need for various other process stages in manufacturing high-efficiency solar cells, silicon nitride (SiNx: H) has recently acquired a unique role in this application. A thin silicon nitride layer is produced on an N/P junction using a plasma-enhanced CVD (PECVD) technique in a typical commercial solar cell production sequence. A nitridation process also produces a positive charge accumulation at the SiN_x:H-Si contact, which aids surface passivation. It also introduces H into Si, which is hidden beneath a thin plasma-damaged surface layer.

3.4 Metallization

For metallization of Si solar cells, the thick film method is employed in the screen-printing process. Evaporation is a manual batch and vacuum process with high facility expenses. The screen-printing technology avoids all these disadvantages with almost the same final efficiency. Furthermore, it is simple to fully automate, resulting in a processing cost savings of 60% to 80%. Metallization pattern is screened on the ARC, which yields an excellent electrical contact, and at the same time, the ARC forms a barrier against the diffusion of impurities into the solar cell. The contact is made when the cell is fire through.

3.4.1 Fire Through Contacts

By screen printing a paste including a cutting agent over the antireflection layer, the metal contacts can attach to the underlying Si. Three things can be affected by firing through. One is the uniformity of front contact formation to have a low resistance to get a high fill factor and V_{oc}. The second one is ohmic contact with high shunt resistivity to get a high J_{SC}. Furthermore, the third one is the diffusion of the hydrogen in the material, and lowering the hydrogen-related impurities and defects and formation of Si-Metal alloyed region to produce low surface recombination to get a high V_{oc}.

3.5 E-Beam Evaporation

During an e-beam evaporation process, the current is first channeled via a tungsten filament, generating joule heating and electron emission. A high voltage is applied between the filament and the hearth to push the emitted electrons towards the crucible containing the material to be deposited. A strong magnetic field concentrates the electrons into a unified beam, which is then transferred to the deposition medium, causing it to evaporate (or sublimate) and deposit onto the substrate. A reactive gas,

such as oxygen or nitrogen, can be introduced to the chamber during evaporation to deposit non-metallic coatings reactively.

There are several advantages to electron beam evaporation versus resistive heat evaporation. For starters, an e-beam source can heat materials to far higher temperatures than a resistive boat or crucible heater. This allows for exceptionally rapid deposition and evaporation of high-temperature materials including refractory metals such as tungsten, tantalum, and graphite. Second, electron beam evaporation films can better retain the purity of the source material because water cooling of the crucible confines electron beam heating to the region covered by the source material, preventing contamination from adjacent components. Finally, single and multi-pocket electron beam evaporation sources are available in a range of sizes and topologies. Pocket indexing uses a motorized carousel to allow a single source to deposit many items from a single location.

3.6 Sample Preparation

The process flow followed in this work is depicted in Figure 20.

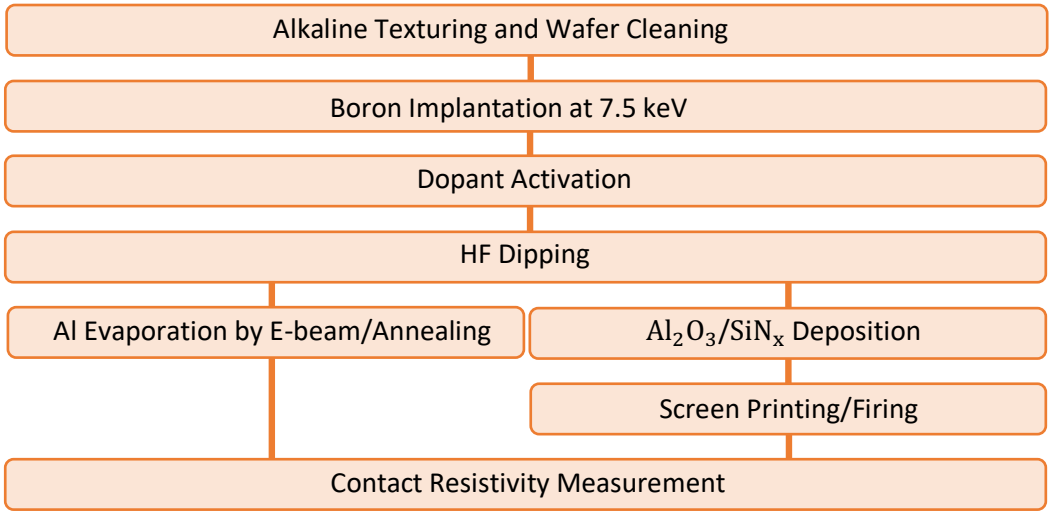

Figure 20. Process flow of sample fabrication.

First, n-type Cz-Si wafers were alkaline textured and ozone cleaned. Then, they were identically implanted with boron ions with an energy of 7.5 keV. After that, the samples went through an annealing process at different temperatures of 950 °C, 1000 °C, and 1050 °C and duration of 30 min and 60 min for dopant activation under N_2 flow. After the samples were HF dipped to remove unintentionally grown oxide, they were divided into two groups. One group was used for Al evaporation by the e-beam method. The schematic of the resulting samples in the first group is shown in Fig.21 (a). The surfaces of the samples in the second group were passivated with Al_2O_3 by atomic layer deposition (ALD) system and subsequently capped with SiN_x deposited by plasma-enhanced chemical vapor deposition (PECVD) tool. Ag/Al paste was screen printed on a boron implanted emitter following the dielectric deposition processes, and a fast-firing process was performed. In this scope, three different firing peak temperatures as 685 °C, 735 °C, and 785 °C, which are measured by a thermocouple attached to the wafer, were applied. The schematic of the resulting samples in the second group is given in Fig.21(b). The ρ_C between the metal contacts and boron implanted emitters was measured with TLM setup. Additionally, each sample's sheet resistances and doping profiles after the HF dipping process were measured by 4PP and ECV methods, respectively.

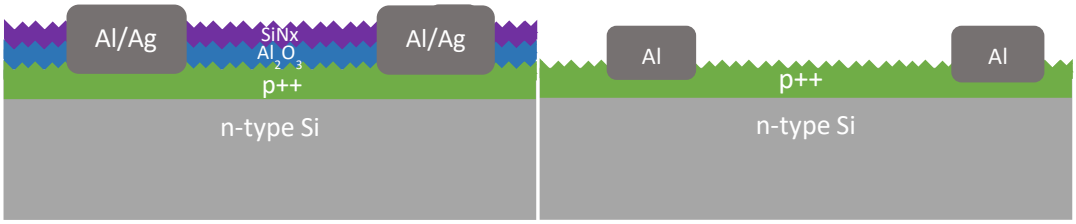

Figure 21. Cross sections of the samples with (a) screen-printing and (b) e-beam evaporated.

CHAPTER 4

RESULTS & DISCUSSION

4.1 Sheet Resistance Results

The series resistance that is distributed to the solar cell is influenced by emitter sheet resistance. Because the FF is influenced by the R_s, the short-circuit current (J_{sc}) is affected, and therefore the efficiency is affected.

Cell efficiency is expected to be high with a higher sheet resistance emitter because of lower recombination losses in the front region of the cells (e.g., emitter and surface). Lower recombination losses in the front of the cells due to lower dopant concentration would lead to higher V_{oc} and I_{sc} but a lower FF. The decrease in FF, which is characteristic of high R_{sheet} emitters, is primarily related to high R_c as the lateral resistance can be minimized by increasing the number of metal lines, once again at the loss of I_{sc}. (Hilali et al., 2004) R_{sheet} ~ 70-75 Ω/sq is the accepted range for better cell performances (Bhosle et al., 2013).

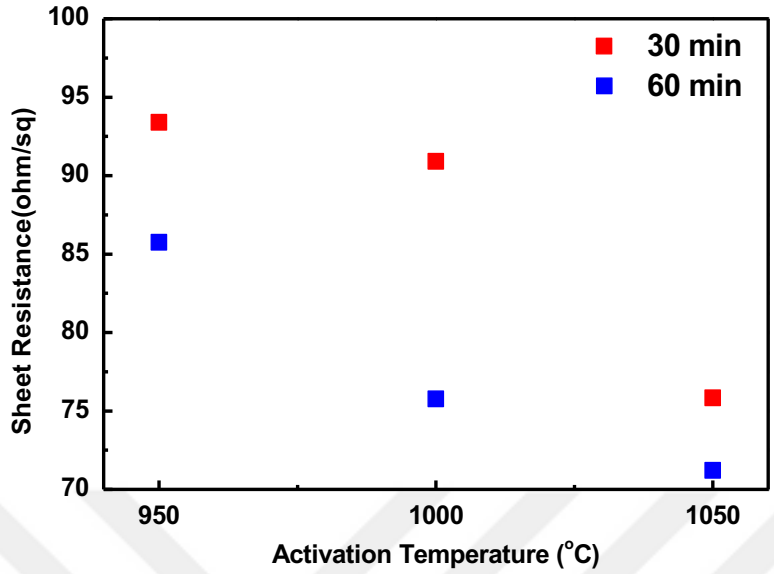

Figure 22. Sheet resistance values over activation temperatures of the samples.

In Figure 22, the activation temperature vs. sheet resistance graph of samples can be seen. The measured R_{sheet} represents only the activated boron ions because the ECV measurements detect only the activated ions. Although it is indicated that boron emitters are activated above 1000 °C (Boo et al., 2012), reaching the ideal R_{sheet} range above 1000 °C was not such a surprise as this result can also be seen in the ECV profile.

4.2 Variation Doping Profile with Activation Process

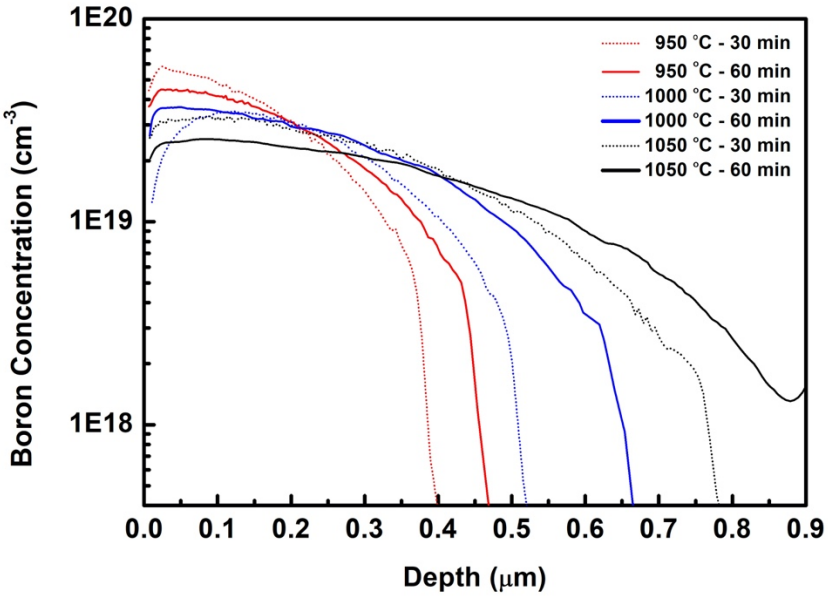

Figure 23. Boron concentration profile of the samples.

Table 3. Samples' calculated dose according to activation time and temperature.

Sample Name	*Activation Time (min)*	*Activation Temperature (°C)*	*Dose Calculated (cm^{-2})*
950 °C-30 min.	30	950	1.19E15
1000 °C-30 min.		1000	1.06E15
1050 °C-30 min.		1050	1.37E15
950 °C-60 min.	60	950	1.17E15
1000 °C-60 min.		1000	1.33E15
1050 °C-60 min		1050	1.28E15

As the activation temperature and time increase, the peak concentration decreases due to the diffusion of boron into the substrate. High concentration annealing is needed to decompose the boron clusters formed during the initial stage of the annealing, which is known to be immobile and electrically inactive (Angelucci et al., 1987). While boron clusters disintegrate around 800 °C, the more stable ones take longer or require greater temperatures (Peterström & Holmén, 1974). This remark suggests that deep junction annealing for boron emitters begins at 1000 °C. Comparing the calculated and measured R_{sheet} (sheet resistance) values, the same result can be seen for the boron emitter as seen in Figure 23.

Calculated sheet resistances, which match the 4PP measurements from the ECV profiles, are seen from Table 4.

Table 4. Calculated sheet resistances of the samples from the ECV measurement.

	950-30	**950-60**	**1000-30**	**1000-60**	**1050-30**	**1050-60**
Sheet Resistance (Ω/sq)	91.24	90.46	96.74	76.99	73.10	75.31

The sheet resistance ρ_{sq} at equilibrium is determined from the net ionised doping concentration N(z) and the mobility of the majority carriers μ_{maj} by the equation

$$\rho_{sq} = \frac{1}{q.\int_0^z \mu_{maj}(z).N(z).dz}$$

where z_j is the junction depth and q is the charge of an electron.

4.3 Contact Resistivity

4.3.1 Screen-Printed Samples

Ag screen-printing metal pastes are commonly used for contacting n^{++} Si layers leading to very ρ_C lower than 5 $m\Omega.cm^2$ (Cabrera et al., 2013). However, they typically result in a high ρ_C above 50 $m\Omega.cm^2$ when contacting p^{++} Si layers {(Lago et al., 2010), (Kopecek et al., 2005), (Kerp et al., 2006), (Riegel et al., 2010)}.

It has been proposed that ρ_C of Si and screen-printed Ag/Al is reduced due to the effect of Al on the growth mechanism of Ag crystallites, which are responsible for contact formation during the firing process. The amount of the Ag crystallites and their sizes significantly increase as the concentration of Al increases in the Ag paste, leading to a decrease in ρ_C {(Lago et al., 2006), (Kerp et al., 2006)}. Additionally, Al in the metallization paste locally dopes the Si. Within these Al-doped areas, contact formation is enhanced (Riegel, 2012).

4.3.1.1 Effect of Sample Width on Contact Resistivity Measurement

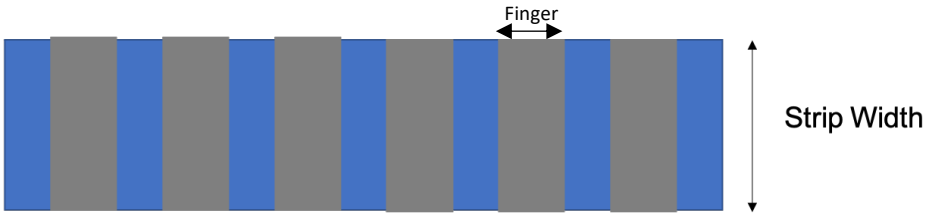

Figure 24. Sample Structure for TLM.

As seen from Figure 24, as the strip width of the sample increases, the measured ρ_C and the transfer length will increase. The poor conductivity of the fingers causes this strip width effect. The conventional TLM theory assumes a two-dimensional model to explain the current flow and ignore finger line resistance. The TLM plot is the relationship between total resistance and the distance between two fingers. Consequently, the part of the total resistance that does not change with distance is

attributed to the contact resistance. The portion of the total resistance that does change with distance is attributed to sheet resistance which can be applied to devices with very narrow strip width or highly conductive fingers. For other cases, the voltage drops down the length of the fingers cannot be ignored, and this voltage drop contributes error to the measured contact resistance (Guo et al., 2017).

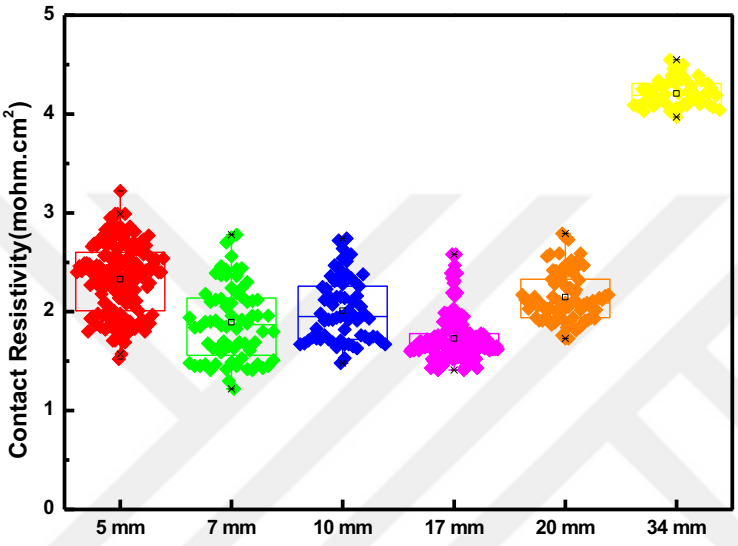

Figure 25. ρ_C vs. sample width.

In Figure 25, we saw that 7 mm, 10 mm, and 17 mm width samples were almost the same while the 5 mm and 34 mm ones have larger ρ_C. Generally, the measured ρ_C should increase as the sample width increases. However, it was found that the 5 mm broad sample did not have the lowest ρ_C. One possibility is that laser cutting induces a shunting effect on the edges of the samples and creates additional shunting paths when the TLM structures are created. Shunt paths increase the measured contact resistance, and this influence becomes more pronounced when the sample width gets smaller. The edge shunting changes the voltage distribution along with the finger. As a result, the voltage change at the end of the finger is much more significant than the typical case, which indicates more current flow from the end of the finger (Guo

et al., 2017). In the case of the 34 nm sample, Guo et al. studied that the voltage change along with the fingers for normal line resistance is much more significant than the ideal case, and this is why higher ρ_C values can be seen for the larger width samples.

In order to reduce the shunting effect and get a minimum errored result, using between 7-17 mm sample can be chosen. We chose the 10 mm sample width for our investigation.

4.3.1.2 Effect of Alumina on Contact Resistivity

The literature shows that the deposition technique applied for alumina can influence the ρ_C dependence with the changing AlO_x thickness (Gapp et al., 2020).

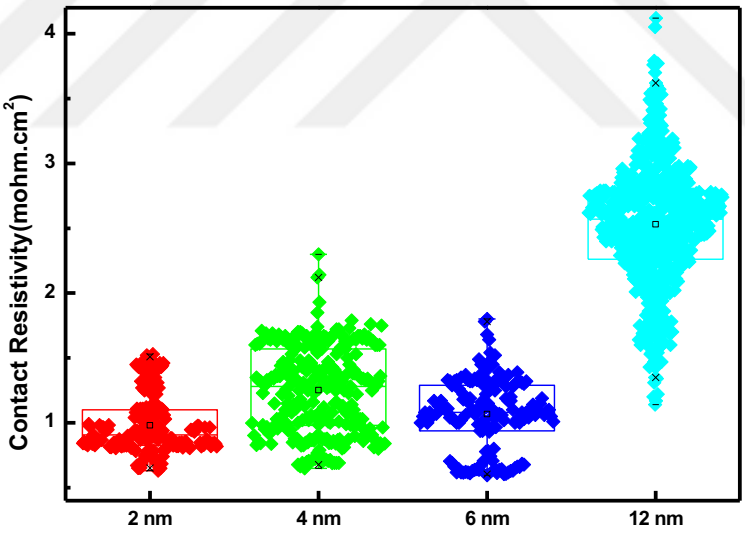

Figure 26. ρ_C between screen printed Al/Ag and implanted p++ with changing alumina thickness.

Alumina thickness influence on contact formation can be explained by the different etching behavior of the glass frit about the increasing amount of Al_2O_3 substituting SiN_y:H in the ARC application-optimized stack. Additionally, this indicates that Al_2O_3 is etched more slowly than SiN_y:H. A longer etching time within the same applied high-temperature step would decrease the available time for Ag crystal formation, leading to increased ρ_c. The Al to O ratio might also impact contact formation (Gapp et al., 2020).

4.3.1.3 Firing Effect on Contact Resistivity

A deeper boron emitter and higher firing temperature may yield a lower ρ_C (Schiele et al., 2014). Three different firing temperatures were examined for this set, and the statement of deeper boron emitter yielding lower ρ_C was tested. The firing temperatures were measured with thermocouples to reflect the accurate temperatures. In Figure 27, firing at 685 °C can be seen.

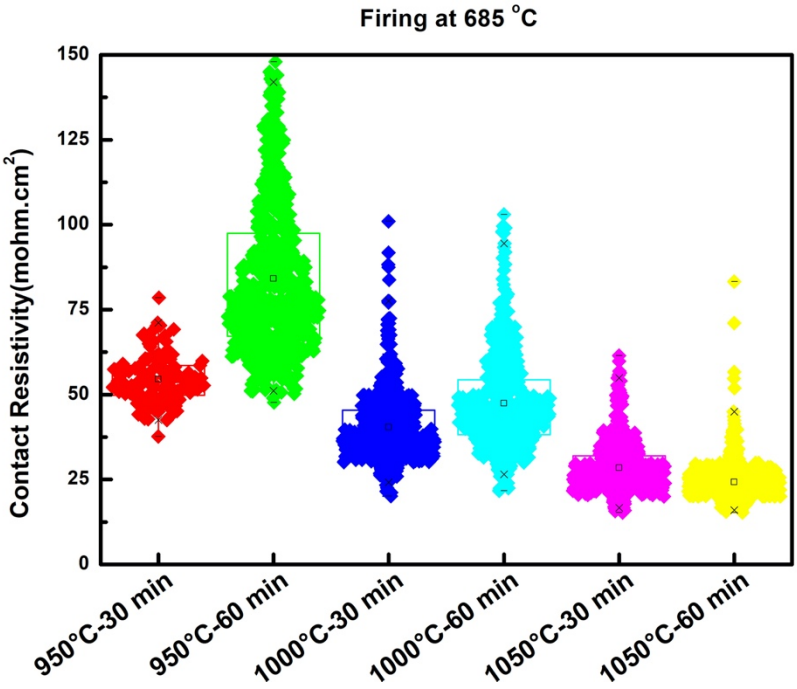

Figure 27. ρ_C values of the samples at firing temperature of 685 °C.

The lower ρ_C value for 685 ºC was achieved at 1050 ºC-60-minute sample, but for the case of 950 ºC, the 30-minute sample had lower ρ_C than the 60-minute one even though it has a shallow boron doping. If we look at the calculated doses from the ECV, they have almost the same amount of dopant. Since the 30-minute sample has a higher surface boron concentration, having a lower ρ_C value from the lower surface boron concentrated sample (950 ºC-60 min) is expected.

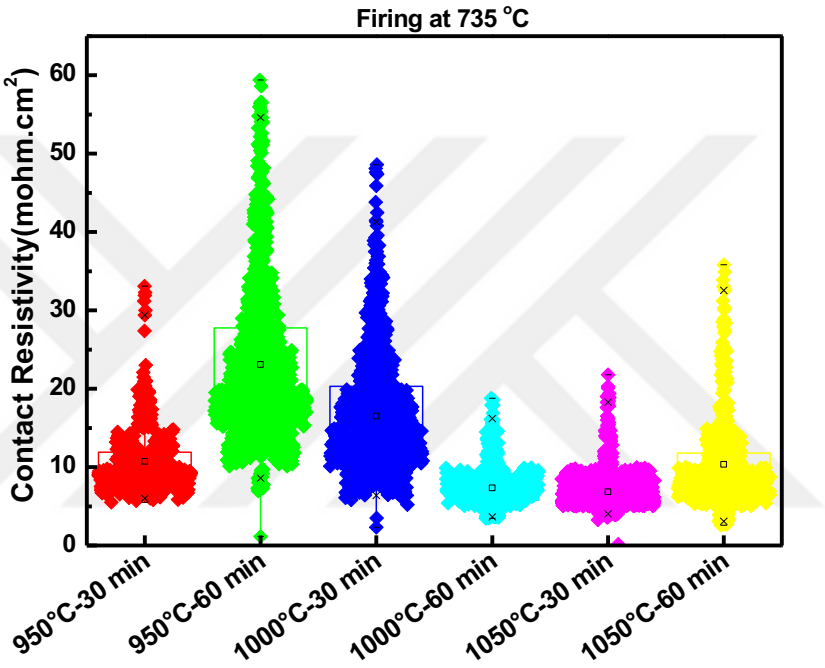

Figure 28. ρ_C values of the samples at firing temperature of 735 ºC.

In Figure 28, the lower ρ_C value was achieved for 1050 ºC-30 minutes sample rather than 1050 ºC 60 minutes sample, since the exposure of samples to high temperatures in both annealing and firing causes a trade-off in ρ_C.

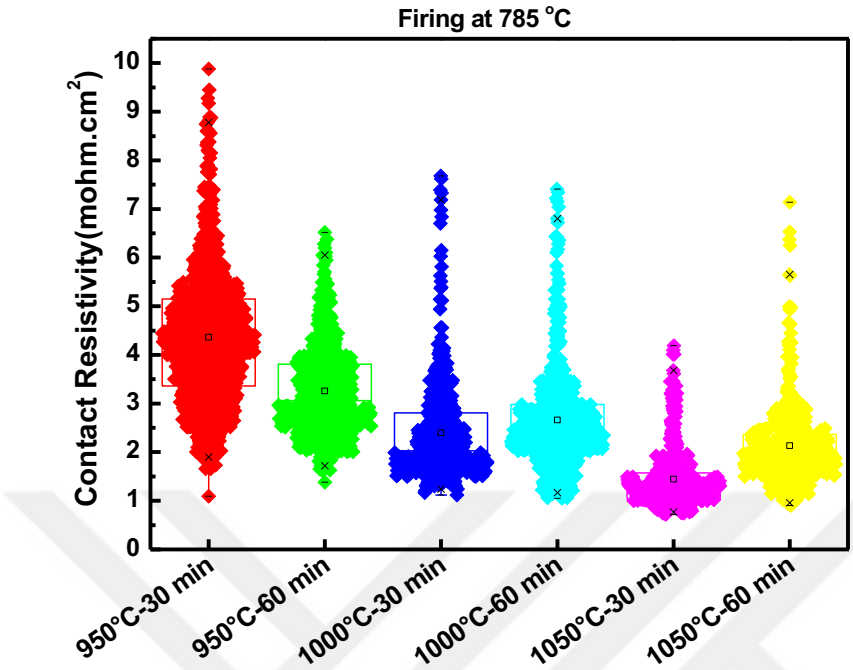

Figure 29. ρ_C values of the samples at firing temperature of 785 ºC.

Because the Ag/Al contact resistance increases with increasing peak processing temperature owing to the thickening of high-resistance Ag-Al alloy layer on the surface Al particles, the similar trade-off is apparent in Figure 29 for 1000 ºC (Zhang et al., 2019). So, we see such a trade-off at high temperatures.

4.3.2 E-Beam Evaporated Samples

The samples were hot-plated after the activation for 5 minutes at 380 ºC.

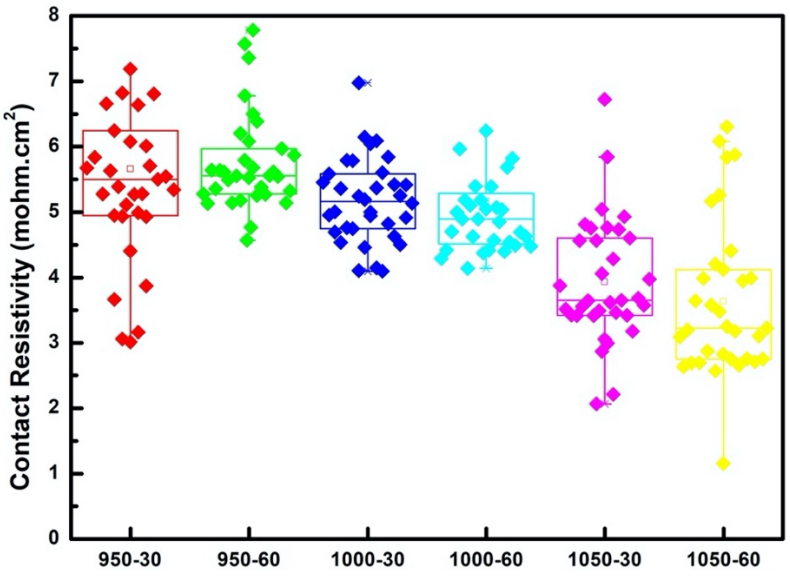

Figure 30. ρ_C values of e-beam evaporated samples.

Comparing the annealing temperatures and durations in Figure 30, the lowest ρ_C is achieved when the samples are annealed at 1050 °C for 60 minutes. The minimum ρ_C value that is achieved was around 3 mΩ.cm^2. From Figure 30, it can be concluded that the ρ_C decreases as the doping profile gets deeper.

Table 5 compares the contact resistivities obtained in the literature and the minimum ones in this study.

Table 5. ρ_C comparison with literature and this study.

	Doping Method	Metallization Method	Metal	ρ_C ($m\Omega.cm^2$)
Mader et al. (2012)	Diffusion	Evaporation	Al	2
Lanterne et al. (2014)	Implantation	Screen Printing	Al/Ag	3.5
Kiefer et al. (2016)	Implantation	Screen Printing	Al/Ag	3.9
Wu et al. (2017)	Diffusion	Screen Printing	Al/Ag	2
Madani et al. (2020)	Diffusion	Screen Printing	Al/Ag	2
This study	Implantation	E-beam	Al	3
This study	Implantation	Screen Printing	Al/Ag	1.5

CHAPTER 5

CONCLUSIONS

In this M.Sc. study, we have investigated the metal contact formation on the emitter of a solar cell prepared by ion implantation. The contact formation has crucial effects on the energy conversion performance of a solar cell. The ion implantation offers precise and straightforward technology for emitter formation in solar cell manufacturing. However, the performance of these emitters needs to be studied from a different point of view. One of the critical parameters is the resistivity of the metal-emitter contact. Also, the effect of sheet resistance of the emitter should be addressed to reach a successful operation. This thesis extensively studied and presented the properties of metal-emitter contact prepared by screen printing and e-beam evaporation.

The uniformity of the boron implantation was first tested with 4PP measurements. ECV measured the doping profiles. The sheet resistance of the samples was uniform, indicating a good uniformity of the ion implantation process. It was observed that as the activation temperature and time increase, the sheet resistance of the samples decreases. Boron ions need to be activated above 1000 ^{o}C to decompose the B clusters, leading to sheet resistance values in the range of 70-75 Ω/sq.

The effect of the activation process on the doping profile was studied. As might be expected, the peak concentration decreases, and the junction depth moves deeper into the substrate with increasing temperature and time. This also affects the sheet resistance of the emitter. The emitter profile needs to be optimized for a high-efficiency solar cell. It is generally desirable to have higher sheet resistance for lower recombination losses in the emitter. However, high sheet resistance in the emitter increases the resistive losses in the emitter and at the metal-emitter junction. So, there

is a trade-off that needs to be addressed here. In order to find the best conditions for a good emitter and its junction with the metal layer, junction properties should be understood with a detailed investigation. This has been the primary goal in this study.

In general, we have observed that the ρ_C of the screen-printed samples decreases with the increasing activation temperature and time. The lowest value of contact resistivities was measured to be 1.5 mΩ.cm2. This value, which is much better than the values required for a good metal contact to the emitter, was obtained from the samples annealed at 1050 ^oC for 30 minutes and fired at 785 ^oC. The reason why we did not see the lowest ρ_C value in the sample annealed longer time (for example, at 1050 ^oC for 60 min.) was simply that Ag/Al contact resistance increases with increasing temperature due to the thickening of high-resistance Ag-Al alloy film on the surface of Al particles. In the case of evaporated Al, the lowest ρ_C value was achieved with the sample 1050-60 as expected since the deepest doping profile can achieve the lowest ρ_C value.

For the passivation of the samples, Al_2O_3 was used. 4 different Al_2O_3 thicknesses were tested, and 4 nm thickness of Al_2O_3 was chosen for detailed experimentation. When metal contact was formed on the Al2O3 layer, ρ_C increases as expected due to the insulating effect of the Al_2O_3 layer. So, again, optimization is needed to benefit from the excellent passivation of the Al_2O_3 layer and obtain the best electrical ρ_C.

For the ρ_C measurements, the TLM method was employed on samples with 1 cm width. Two different metallization methods were studied in this M.Sc. work: the first one is the screen-printing and the second one is the e-beam evaporation. Three different firing temperatures have been experimented with for the screen-printed samples, and for the e-beam evaporated samples, 380 ^oC annealing was implemented at the hot plate to obtain good ohmic behavior.

In conclusion, we have succesfuly demonstrated a good metal-emitter contact formation for the ion implanted emitter in this work. We have achived excellent ρ_C values as low as 1.5 mΩ.cm^2 on boron implanted samples. However, if the metallization is made by screen-printing, the Ag-Al alloy film on the top of Al particles should be considered since it contradict with the idea of deeper boron junction leads to the lowest ρ_C. However, in the case of e-beam evaporated sample, it can be seen that indeed deeper boron junction leads to the lowest ρ_C and the achieved minimum ρ_C value was around 3 mΩ.cm^2. It is also investigated that the effect of doping profile on the ρ_C between evaporated Al and boron implanted n-Si wafer. Due to the mask used during evaporation, the sample width is 10 mm, the finger distance is 17,5 mm, and finger openings are 2.5 mm.

The active doping profile varied by activation temperature and time and affected the contact quality of evaporated Al by the e-beam system. As the doping profile gets deeper, the ρ_C decreases. In this study, we have achieved an excellent ρ_C value of around 1.5 mΩ.cm^2 for the sample activated at 1050 ^{o}C for 30 min.

In the future, the effect of doping profile on emitter quality and the influence of these doping profiles and contact resistivities on solar cell performance will be investigated.

REFERENCES

Aissa, B., Kivambe, M., Hossain, M., Daif, O., Abdallah, A., Ali, F., & Tabet, N. (2015). Emerging frontiers of N-Type silicon material for photovoltaic applications: The impurity-defect interactions. *Frontiers in Nanoscience and Nanotechnology*.

Angelucci, R., Cembali, F., Negrini, P., Servidori, M., & Solmi, S. (1987). Temperature and Time Dependence of Dopant Enhanced Diffusion in Self-Ion Implanted Silicon. *J. Electrochem. Soc. : Solid-State Science and Technology*, *134*(12), 3130–3134.

Bahar H., Bojek B. (2020) Solar PV. IEA web page: https://www.iea.org/reports/solar-pv

Bera, C. (2010). Thermo electric properties of nanocomposite materials (Doctoral dissertation, Ecole Centrale Paris).

Bhosle, V., Tsefrekas, B., Gossmann, H. J. L., & Dube, C. E. (2013). Fabricating high efficiency solar cells with high sheet resistance emitters by ion implantation and contact resistance modeling. *Conference Record of the IEEE Photovoltaic Specialists Conference*, 2167–2170.

Boo, H., Lee, J. H., Kang, M. G., Lee, K., Kim, S., Hwang, H. C., Hwang, W. J., Kang, H. O., Park, S., Tark, S. J., & Kim, D. (2012). Effect of high-temperature annealing on ion-implanted silicon solar cells. *International Journal of Photoenergy*. https://doi.org/10.1155/2012/921908

Buck, T., & NEJATI, J. (2014). Engineering and Characterization of Metal Contacts to P+ Doped Silicon. In EU PVSEC Proceedings. Amsterodam: 29th European Photovoltaic Solar Energy Conference and Exhibition (pp. 401-405).

Cabrera, E., Olibet, S., Rudolph, D., Wefringhaus, E., Kopecek, R., Reinke, D., &

Schubert, G. (2012). Influence of surface topography on the glass coverage in the contact formation of silver screen-printed Si solar cells. *IEEE Journal of Photovoltaics*, 3(1), 102-107.

Carrier Mobility semiconductors. (2010). http://conocimientoscarriertransport.blogspot.com/2010/06/carrier-mobility-semiconductors.html

Chodos, A. (2009, April). *This month in physics history*. American Physical Society. https://www.aps.org/publications/apsnews/200904/physicshistory.cfm.

Dreike, P. L., Fleetwood, D. M., King, D. B., Sprauer, D. C., & Zipperian, T. E. (1998). An overview of high-temperature electronic device technologies and potential applications. *High-Temperature Electronics*, *17*(4). https://doi.org/10.1109/9780470544884.ch3

Electrochemical CV-Profiling. (n.d.). https://probion.fr/ecv-en/

Fritz, S., König, M., Riegel, S., Herguth, A., Hörteis, M., & Hahn, G. (2014). Formation of Ag/Al screen-printing contacts on B emitters. *IEEE Journal of Photovoltaics*, 5(1), 145-151.

Gapp, B., Geml, F., Engelhardt, J., & Hahn, G. (2020). A study on the influence of aluminium oxide layer properties on contact formation. *37th European Photovoltaic Solar Energy Conference and Exhibition (EUPVSEC)*, 525–528.

Green, M. A. (2009). The Path to 25% Silicon Solar Cell Efficiency: History of Silicon Cell Evolution. *Progress in Photovoltaics: Research and Applications*, *17*(3), 183–189. https://doi.org/10.1002/pip

Green, M. A. (2015). Crystalline silicon solar cells. In *Crystalline Silicon Solar Cells*.

Guo, S., Gregory, G., Gabor, A. M., Schoenfeld, W. V., & Davis, K. O. (2017).

Detailed investigation of TLM contact resistance measurements on crystalline silicon solar cells. *Solar Energy*, *151*, 163–172. https://doi.org/10.1016/j.solener.2017.05.015

Hieslmair, H., Mandrell, L., Latchford, I., Chun, M., Sullivan, J., & Adibi, B. (2012). High Throughput Ion-Implantation for Silicon Solar Cells. *Energy Procedia*, *27*, 122–128.

Hilali, M. M., Rohatgi, A., & Asher, S. (2004). Development of screen-printed silicon solar cells with high fill factors on 100 Ω/sq emitters. *IEEE Transactions on Electron Devices*, *51*(6), 948–955. https://doi.org/10.1109/TED.2004.828280

Honsberg C.B., & Bowden S.G. (2019). *Photovoltaics Education Website*. https://www.pveducation.org/

Hubbard, S. (2016). Recombination. In A. Reinders, P. Verlinden, W. van Sark, & A. Freundlich (Eds.), *Photovoltaic Solar Energy: From Fundamentals to Applications* (pp. 39–46).

Hull, R. (1999). *Properties of Crystalline Silicon*.

Huyeng, J. D., Efinger, R., Bruge, D., Spribille, A., Wolf, A., Keding, R., ... & Clement, F. (2019, August). Towards all screen printed back-contact back-junction silicon solar cells. In *AIP Conference Proceedings* (Vol. 2147, No. 1, p. 070005). AIP Publishing LLC.

Jinko Solar. (2020). *JinkoSolar Large-Area N-Type Monocrystalline Silicon Solar Cell Reaches Record High Efficiency of 24.79%.*

Kerp, H., Kim, S., Lago, R., Recart, F., Freire, I., Pérez, L., ... & Shaikh, A. (2006). Development of screen printable contacts for p+ emitters in bifacial solar cells. *Proc. 21st EU PVSEC Dresden*, 892-4.

Kiefer, F., Krügener, J., Heinemeyer, F., Jestremski, M., Osten, H. J., Brendel, R., & Peibst, R. (2016). Bifacial, fully screen-printed n-PERT solar cells with

BF2 and B implanted emitters. *Solar Energy Materials and Solar Cells*, 157, 326-330.

Kopecek, R., Buck, T., Libal, J., Petres, R., Röver, I., Wambach, K., ... & Fath, P. (2005). Large area n-type multicrystalline silicon solar cells with B-emitter: efficiencies exceeding 14%. *Proc. 15th IPSEC, Shanghai*, 883-4.

Lago, R., Pérez, L., Kerp, H., Freire, I., Hoces, I., Azkona, N., Recart, F. and Jimeno, J.C. (2010), Screen printing metallization of boron emitters. Prog. Photovolt: Res. Appl., 18: 20-27.

Lanterne, A., Le Perchec, J., Gall, S., Coig, M., Tauzin, A., & Veschetti, Y. (2014). 20.5% efficiency on large area n-type PERT cells by ion implantation. *Energy Procedia*, 55, 437-443.

Lohmüller, E., Werner, S., Hoenig, R., Greulich, J., & Clement, F. (2015). Impact of boron doping profiles on the specific contact resistance of screen printed Ag–Al contacts on silicon. *Solar Energy Materials and Solar Cells*, 142, 2-11.

Madani, K., Rohatgi, A., Min, K. H., Song, H. E., Huang, Y. Y., Upadhyaya, A. D., ... & Ok, Y. W. (2020). Comparison of passivation properties of plasma-assisted ALD and APCVD deposited Al2O3 with SiNx capping. *Solar Energy Materials and Solar Cells*, 218, 110718.

Mader, C., Müller, J., Eidelloth, S., & Brendel, R. (2012). Local rear contacts to silicon solar cells by in-line high-rate evaporation of aluminum. Solar energy materials and solar cells, 107, 272-282.

Mah, O. (1998). *Fundamentals of photovoltaic materials*.

Meyers, G. (2014). *Photovoltaic Dreaming 1875–1905: First Attempts At Commercializing PV*.

Nelson, J. (2003). *The physics of solar cells*. London: Imperial College Press.

Nishinaga, T. (2015). *Handbook of Crystal Growth: Fundamentals* (Second Edi).

Elsevier.

O'Donnell, K. P., & Chen, X. (1991). Temperature dependence of semiconductor band gaps. *Applied Physics Letters*, *58*(25), 2924–2926. https://doi.org/10.1063/1.104723

Obeid, K. (2010). *Preparation and Study Some of Electrical and Thermal Properties of a Nematic Liquid Crystal Material Prepared from Schiff Bases and Some its Complexes*. Babylon University.

Peterström, S., & Holmén, G. (1974). Isothermal annealing of boron implanted Silicon. *Physica Scripta*, *10*(3), 142–144. https://doi.org/10.1088/0031-8949/10/3/009

Plakhotnyuk, M. (2018). *Nanostructured Heterojunction Crystalline Silicon Solar Cells with Transition Metal Oxide Carrier Selective Contacts*. DTU Nanotech.

Rane, B., Khanna, P. ., Seth, T., Phatak, G. ., Amalnerkar, D. ., & Das, B. . (2003). Firing and processing effects on microstructure of fritted silver thick film electrode materials for solar cells. *Materials Chemistry and Physics*, *82*(1), 237–245.

Recart, F., Freire, I., Perez, L., Lago-Aurrekoetxea, R., Jimeno, J. C., & Bueno, G. (2007). Screen printed boron emitters for solar cells. *Sol.Energy Mater. Sol. Cells*, *91*, 897–902.

Rhoderick, E. H. (1982). Metal-semiconductor contacts. *IEE Proc*, *129*(1).

Riegel, S., Mutter, F., Lauermann, T., Terheiden, B., & Hahn, G. (2012). Review on screen printed metallization on p-type silicon. Energy Procedia, 21, 14-23.

Sah, C.-T. (2006). *Fundamentals of solid state electronics*. Singapore: World Scientific.

Schiele, Y., Hahn, G., & Terheiden, B. (2014). Contacting and recombination analysis of boron emitters via etch-back for advanced n-type Si solar cells. *In*

European Photovoltaic Solar Energy Conference and Exhibition; 29 (pp. 825-829).

Schmidt, J., Merkle, A., Bock, R., Altermatt, P. P., Cuevas, A., Harder, N., Hoex, B., Sanden, R. Van De, Kessels, E., & Brendel, R. (2008). Progress in the Surface Passivation of Silicon Solar Cells. *Solar Energy*, *September*, 974–981. http://www.isfh.de/institut_solarforschung/files/val08_schmidt.pdf

Schubert, G. (2006). Thick film metallisation of crystalline silicon solar cells: Mechanisms, models and applications (Doctoral dissertation).

Uddin, J. (2019). Effect of doping profile on sheet resistance and contact resistance of monocrystalline silicon solar cells. *Materials Research Express*, *6*.

Ur Rehman, A., & Lee, S. H. (2013). Advancements in n-type base crystalline silicon solar cells and their emergence in the photovoltaic industry. *The Scientific World Journal*, *2013*. https://doi.org/10.1155/2013/470347

Wu, W., Roelofs, K. E., Subramoney, S., Lloyd, K., & Zhang, L. (2017). Role of aluminum in silver paste contact to boron-doped silicon emitters. *AIP Advances*, 7(1), 015306.

Zeghbroeck, B. Van. (2010). *Contact resistance to a thin semiconductor layer*. https://ecee.colorado.edu/~bart/book/book/chapter3/pdf/ch3_5_4.pdf

Zhang, J., Yuan, X., Tong, H., Yang, Y., Zhao, H., & Li, H. (2019). Effect of glass phase and temperature on contact resistance between Ag and Al electrodes. *Materials Research Express*, *6*(3). https://doi.org/10.1088/2053-1591/aaf52b